

Characterizing CO₂ plumes in deep saline formations: Comparison and joint evaluation of time-lapse pressure and seismic tomography

Linwei Hu¹, Joseph Doetsch¹, Ralf Brauchler², and Peter Bayer³

ABSTRACT

Monitoring the migration of sequestered CO₂ in deep heterogeneous reservoirs is inherently difficult. Geophysical methods have been successfully used, but flow conditions are only indirectly linked to the measured properties. Besides geophysical methods, pressure tomography (PT) is proposed as an alternative method to depict the structure of deep saline formations for CO₂ sequestration and to continuously delineate CO₂ plumes. In contrast to more established geophysical measurements, pressure transients are directly related to flow properties, which allows for the estimation of permeability. We investigate the influence of aquifer heterogeneity on PT performance, and we compare the PT results to crosshole seismic tomography (ST). Multilevel fluid injections and high-frequency P-wave pulses are induced in a simulated deep

borehole, and the recorded signals at another well are processed by a traveltime inversion scheme. The reservoir structure is inferred by clustering the inverted hydraulic diffusivity prior to CO_2 injection, and the plume distribution is determined by clustering the tomograms of the inverted mixed-phase diffusivity difference and P-wave velocity difference. The clustered structures are then used for zonal calibration to acquire the saturation within the plumes. Modeling results indicate that PT provides clearer structural information on the CO_2 -free aquifer due to its direct linkage to permeability. However, the plume depicted by PT can be ambiguous, whereas ST is less sensitive to the prevailing heterogeneity of permeability at postinjection and can thus image the plume more clearly. PT and ST can be complementary to each other through the joint clustering to improve plume shape identification and estimation of spatial CO_2 saturation.

INTRODUCTION

A recent report (Global CCS Institute, 2015) pointed out that CO₂ capture and storage (CCS) is the only countermeasure to lessen greenhouse gas emissions in a significant scale from industrial processes. Among various geologic storage media, deep saline aquifers are considered sound formations for sequestering CO₂, in which CO₂ is injected and stored in a supercritical state, with a large storage capacity. Safe disposal of CO₂ in saline aquifers demands favorable storage conditions, such as high porosities in the storage medium and an impermeable caprock. In case of unfavorable conditions, such as seal imperfections, preexisting faults or overpressure-induced fractures, an evolving CO₂ plume can escape toward shallower formations and, which might have an adverse impact on shallow groundwater quality (Wang and Jaffe, 2004). For minimizing the risk

of CO₂ leakage and for formulating effective remediation strategies, appropriate site investigation and CO₂ plume monitoring techniques are required.

Geophysical exploration methods are extensively applied for depicting stratigraphy and CO_2 plume geometry in deep saline formations. Their applicability has been demonstrated at several CO_2 storage sites, such as Sleipner (Chadwick et al., 2010), Snøhvit (Shi et al., 2013), In Salah (Ringrose et al., 2009), Ketzin (Zhang et al., 2012), Cranfield (Doetsch et al., 2013), Frio brine pilot (Daley et al., 2011), and Nagaoka (Nakajima et al., 2014). The most common geophysical approaches for monitoring of CO_2 plumes are seismic surveys, electrical methods, and gravity measurements. The induced CO_2 phase alters the effective physical properties of the storage formation (e.g., seismic velocity, electrical resistivity, and density) over time, which is examined by time-lapse data sets.

Manuscript received by the Editor 12 July 2016; revised manuscript received 18 March 2017; published ahead of production 2 May 2017; published online 19 June 2017.

¹ETH Zurich, Department of Earth Sciences, Zurich, Switzerland. E-mail: linwei_hu@outlook.com; joseph.doetsch@erdw.ethz.ch.

²AF-Consult Switzerland Ltd., Baden, Switzerland. E-mail: ralf.brauchler@afconsult.com.

³Ingolstadt University of Applied Sciences, Institute of New Energy Systems (InES), Ingolstadt, Germany. E-mail: peter.bayer@thi.de. © 2017 Society of Exploration Geophysicists. All rights reserved.

ID2 Hu et al.

Among established geophysical techniques, active seismic surveys are most commonly used. Usually, seismic measurements are conducted prior to CO₂ injection to obtain baseline information, and then measurements are repeated multiple times after CO₂ injection. CO₂ plume evolution is monitored by the traveltime delay or amplitude anomalies from different vintages. Depending on the configurations of sources and receivers, seismic-based approaches can be classified into the surface seismic survey, surface-downhole monitoring, and crosshole measurement. Typically, a 2D or 3D surface seismic survey is conducted for large-scale problems, and its spatial resolution is limited. In the case that the CO₂ layer thickness is less than the resolution, the uncertainty for evaluating the CO₂ mass becomes significant (Ivandic et al., 2015). Surface-downhole monitoring includes two different configurations, namely, vertical seismic profiling and moving-source-profiling. It is used for estimating the vertical expansion of the CO₂ plume and for improving the vertical resolution to complement surface seismic methods. For crosshole measurements, the seismic sources and receivers are installed in different boreholes, and the experiments are performed for obtaining insight in the reservoir and mapping CO₂ plumes between the borehole pair. The crosshole variant can provide high-resolution information between the boreholes, which are typically separated by a distance of tens to hundreds of meters. The main inversion algorithms for crosshole seismic tomography include traveltimebased and full-waveform inversion (Pratt and Shipp, 1999).

Although successful at imaging migrating CO₂, two difficulties have been identified for established geophysical approaches. First, petrophysical models have to be formulated for analyzing the stored CO₂ in the subsurface, which is challenging mainly due to the uncertainty in model parameters. For instance, for a petrophysical model that couples a patchy fluid-saturation model, the patch size of CO₂ is difficult to determine precisely in practice (Daley et al., 2011). Second, favorable conditions are required for the repeatability of geophysical experiments, such as a high contrast of reservoir properties, identical experimental setups at different times, and low noise levels. Not having these ideal conditions can lead to artifacts during inversion of time-lapse data sets, or during conversion of geophysical parameters into CO₂ saturation.

As a complementary method for characterizing reservoir and monitoring CO2 plumes during the early time of storage, as well as for detecting CO₂ leakage, pressure-based methods have recently been suggested. Because pressure directly relates to flow conditions and travels much faster than a CO2 plume, pressure-based methods are recognized as an appropriate approach for evaluating the flow properties before and during CO₂ injection (Doughty et al., 2008; Wiese et al., 2010), as well as for early detection of CO₂ leakage (Birkholzer et al., 2009; Sun et al., 2016). However, few pressure-based methods can provide a spatial image of CO₂ plumes. Several available techniques can identify the plume shape to a certain degree. For instance, the upconing of a CO2 plume near the well or a CO2 front can be inferred by some analytical or semianalytical solutions (Nordbotten et al., 2004; Cihan et al., 2011). The approach of Martinez-Landa et al. (2013) can estimate the proximal width of a CO₂ plume by analyzing pressure measurements in a single borehole. Nevertheless, most of these methods are based on the assumption that the reservoir is homogeneous, neglecting most of the involved physicochemical CO₂ transport processes and potential reservoir heterogeneity.

For resolving spatial variability of flow properties, hydraulic tomography (HT) was proposed by Gottlieb and Dietrich (1995)

and has seen significant development since its introduction. Compared with conventional hydraulic/pressure tests, HT can delineate the spatial distribution of hydraulic parameters. Feasibility of HT has been studied in porous (Yeh and Liu, 2000; Hu et al., 2011; Cardiff et al., 2013; Paradis et al., 2015) and fractured media (Hao et al., 2008; Illman et al., 2009; Sharmeen et al., 2012; Zha et al., 2014) by numerical simulations (Zhu and Yeh, 2005; Jiménez et al., 2013; Schwede et al., 2014), laboratory experiments (Brauchler et al., 2007; Liu et al., 2007; Zhou et al., 2016), and field tests (Straface et al., 2007; Brauchler et al., 2013; Jiménez et al., 2015; Zha et al., 2015). The application scale of HT can vary from several meters to kilometers. The rationale of HT is conceptually analogs to geophysical tomographic techniques. In lieu of using geophysical sources (e.g., active or passive seismic excitations), HT or more generally pressure tomography (PT), requires a series of pressure stimulations in a tomographic array. Tomographic data sets are derived by conducting fluid injection or extraction tests in different intervals at one well (sources), with pressures measured at the response well at different observation levels (receivers). The pressure measurements are used for reconstructing hydraulic parameter heterogeneity by different inversion techniques, such as the sequential successive linear estimator (Yeh and Liu, 2000), quasilinear Bayesian geostatistical method (e.g., Nowak and Cirpka, 2004), ensemble Kalman filter (Schöniger et al., 2012), and the traveltimebased approach (Brauchler et al., 2003). Most of the available HT inversion techniques are based on predefined geostatistical models with known or presumptive correlation lengths and variances of hydraulic parameters. These models are taken to generate hydraulic parameter fields and then to simulate the groundwater flow during an iterative inversion procedure. On the contrary, the traveltime-based inversion approach does not require geostatistical estimates, and the inversion process does not involve flow modeling. Instead, the groundwater flow equation is approximated to an eikonal equation, which can be solved in a computational efficient way by the ray-tracing technique (Jackson and Tweeton, 1996). Structural information of the aquifer is then inferred from reconstructed diffusivity tomograms.

To date, HT methods are mainly applied to the "static" singlephase flow condition (i.e., hydraulic parameters are considered not varying with time) and shallow aquifers. Hu et al. (2015) introduce the concept of "time-lapse PT." It is proposed to use the traveltime-based inversion strategy for identifying an evolving CO₂ plume in a homogeneous deep saline aquifer. In this case, replacement of the local brine by CO2 induces an effect on the observed flow properties over time. Considering CO₂ and brine as a phase mixture, the mixed-phase diffusivity can be changed by up to two orders of magnitude due to the high compressibility of CO2. Spatial diffusivity variations can be inferred from inspecting pressure transients at different times. Thus, the inversion of traveltimes derived from pressures offers time-lapse information of the plume. Furthermore, CO₂ saturation can be estimated by including a storativity-saturation model. In comparison with geophysical approaches, PT is not related to the CO₂ plume or patch size because it considers CO₂ and brine as a mixture (Hu et al., 2015). The properties of the CO₂-brine mixture are estimated from the density, viscosity, and temperature.

As mentioned above, previous study on time-lapse PT in Hu et al. (2015) was based on a homogeneous aquifer, without considering data noise and formation heterogeneity. The main objective of this study is to further explore the inversion performance of PT in heterogeneous formations and to compare the results with those from cross-

hole traveltime seismic tomography. In contrast to seismic traveltime tomography, two-phase PT is unusual for such conditions. Due to the direct and more deterministic relationship between CO_2 saturation and hydraulic properties, such as storativity, it is anticipated that PT can complement existing seismic approaches through the improved estimation of saturation. In the following section, we first briefly introduce the two tomographic inversion concepts used in a time-lapse manner. These are examined together in scenarios with different degrees of heterogeneity. For simplification, the expression "seismic tomography" mentioned in this study refers to the traveltime-based seismic tomography method.

ing computing efficiency, the caprock and seal bottom are assumed to be impervious and considered to be no-flow boundaries during flow simulation. The lateral extension of the entire model is 580 m, which is bounded with constant hydrostatic pressure at the east and west sides. The pressure at the model bottom is 14.76 MPa, with a pressure gradient of 0.01 MPa/m. The aquifer is initially fully saturated with brine, and its temperature and salinity are 67°C and 67 g/l, respectively. Under these conditions, CO_2 is injected and sequestered in a supercritical state.

METHODOLOGY

Overview of the methodology

In this work, the inversion methodology is tested using real site-based synthetic models. As a basis, we set up three scenarios for this synthetic model, which differ with respect to heterogeneity and model parameters. Subsequently, we investigate the changes of the mixed-phase diffusivity and P-wave velocity induced by CO₂ injection. The relationship between either diffusivity or velocity and CO₂ saturation provides the basis for the inversion.

Figure 1 presents the general flowchart of the forward simulation, inversion, and calibration procedures. The CO2 sequestration process is simulated with a fully coupled two-phase simulator, PFLOTRAN (Hammond et al., 2014). PT and ST data acquisition is simulated prior to and after CO₂ injection. The derived hydraulic and seismic traveltimes are inverted separately to reconstruct the spatial distribution of diffusivity and velocity. The structure of the reservoir and the geometry of the CO₂ plume are obtained by individual or joint clustering (JT) of the tomograms at different times. Ultimately, we acquire the CO₂ saturation through the calibrated specific storage based on the clustered structure, and the calibration is conducted in a single-phase emulator. In the following sections, each step is explained in detail.

Problem setup

Virtual site and three scenarios

A simplified 2D cross-sectional model based on a virtual site is used for testing our method (as in Hu et al., 2015, 2016). The simulated regime is located at a depth of 1600 m, constituting three components: a storage reservoir, an overlying caprock, and an underlying bottom seal (Figure 2). The thickness of the reservoir and the two low-permeability components are 15 and 30 m, respectively. The reservoir is composed of sandstone, and the caprock and bottom seal are shale formations with very low permeability. We assume that initially no CO₂ exists in the reservoir. For improv-

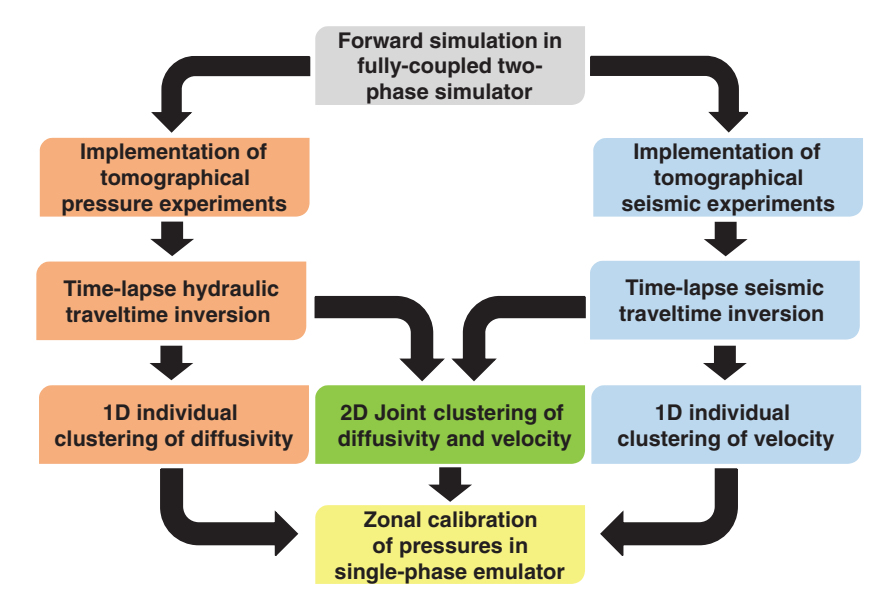


Figure 1. Schematic flowchart of the forward simulation, inversion, and calibration strategy.

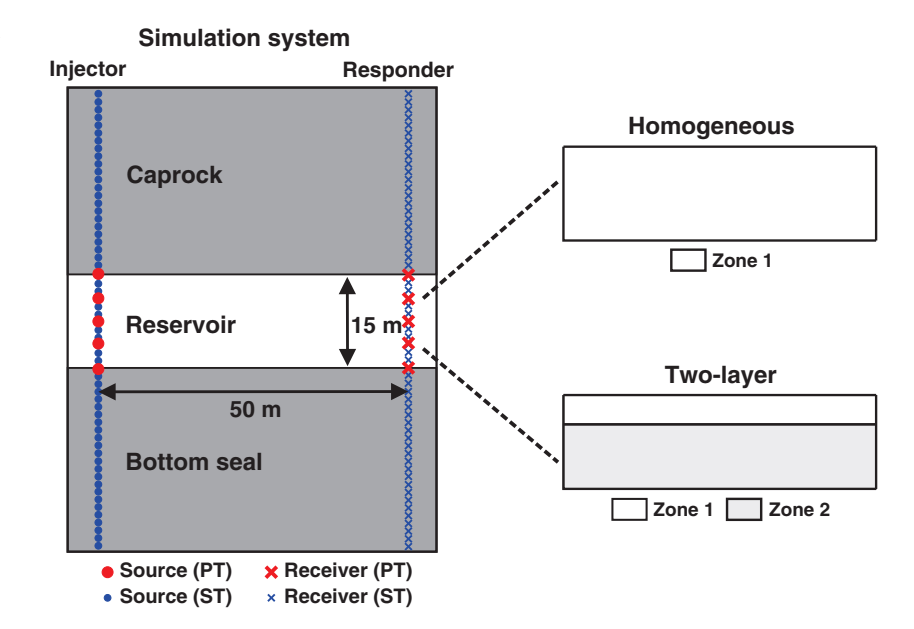


Figure 2. Conceptual model and source-receiver configurations of PT and ST. The left figure only presents part of the model. For details of the full model, the reader is referred to Figure A-1. Three variants of aquifer heterogeneity, one homogeneous, and two two-layer scenarios are considered. Note that sources and receivers for ST are illustrated schematically, and their true numbers are much higher (76).

ID4 Hu et al.

The fluid injection well is at the center of the model (see Appendix A), fully penetrating the entire aquifer. An accompanying observation well is located 50 m away. The distance between the well pair is comparable to several practical injection sites such as Ketzin (Wiese et al., 2010) and Heletz (Niemi et al., 2016). The lateral grid size of the model increases telescopically, ranging from 0.09 m at the injector to 40 m at the side boundaries. The vertical discretization of the model is 0.6 m. Finally, the model is discretized by 287 and 75 grid cells in the horizontal and vertical directions, with 21,525 grid cells in total (see Appendix A).

For PT, five sources and five receivers are used. These are screened at injection and observation wells in the reservoir (Figure 2, red circles and crosses). The length of each source (fluid injection interval) is 0.6 m, and the distance between two adjacent sources or receivers is 3.6 m. To formulate a tomographic configuration, fluid is injected sequentially at the five sources. During each injection, pressure fluctuations at all five receivers are monitored simultaneously. Sources and receivers for ST are also assumed to be located at the two wells (sources are in the injection well, and receivers are in the observation well). The distribution of sourcereceiver configurations for ST experiments is much denser (Figure 2, blue circles and crosses). Here, 76 sources and 76 receivers are installed referring to Ajo-Franklin et al. (2013). The number of seismic sources and receivers is much more than pressure sources and receivers. This is because the installation of borehole isolation systems (e.g., packers, multichamber systems) is needed for PT. Seismic sources and receivers are not only in the reservoir but are also in the caprock and bottom seal, which allows locating a reservoir prior to conducting pressure tests. This also yields larger angle tomographic arrays to improve spatial resolution. The vertical distance between two adjacent seismic sources or receivers is 1 m.

Three different scenarios are defined for exploring the influence of reservoir heterogeneity. In the first scenario, the reservoir is perceived as a homogeneous and isotropic aquifer. In the second and third scenarios, the reservoir consists of two "perfect" homogeneous and

isotropic layers (Figure 2). The thickness of the upper and lower layers is 5 and 10 m, respectively. We discriminate these two scenarios by assigning different values of model parameters (permeability, porosity, and other parameters calculated by these) for the two layers. In the next sections, we refer to these three scenarios as "homogeneous," "2layers_A," and "2layers_B," with 2layers_A having the higher permeability in the upper layer and 2layers_B in the lower layer.

Model parameters

Model parameters are summarized in Tables 1 and 2. The values of model parameters for the homogeneous scenario are the same as in Hu et al. (2015). The intrinsic permeability k, porosity ϕ , and rock density ρ_r are 1×10^{-13} m², 0.23, and 2550 kg/m³, respectively. Rock density ρ_r is estimated by the rock-matrix density ρ_m , brine density ρ_w , and porosity ϕ through equation B-4. The values of ρ_m and ρ_w are 3000 and 1052 kg/m³, respectively.

The characteristic functions of permeability-saturation and capillary pressure-saturation are based on the Brooks-Corey-Burdine model (Burdine, 1953; Brooks and Corey, 1964). The pore-size distribution λ and entry pressure P_d are set to 0.76 and 4000 Pa, respectively.

In the scenario 2layers_A, the permeability of the top layer is 1×10^{-12} m² and the bottom layer is 1×10^{-13} m². The corresponding ϕ is set to 0.28 and 0.22, which is calculated from k according to an empirical equation for sandstone (Schön, 2011)

$$k = 3.95 \times 10^{-17} \cdot \exp(35.77\phi).$$
 (1)

The pore-size distribution λ is set to a constant value of 1.5 for the entire model. The P_d is calculated by the Leverett scaling function (Leverett, 1941), which explains the difference in k, ϕ , and P_d between a reference and an unknown media

$$P_{d} = \frac{\sqrt{\frac{k_{\text{ref}}}{\phi_{\text{ref}}}}}{\sqrt{\frac{k}{\phi}}} P_{d,\text{ref}}, \tag{2}$$

Table 1. Parameter values of numerical model based on a virtual site.

Parameter	Value	Reference
Intrinsic permeability of the caprock and seal bottom (k_{cap} and k_{seal})	$1 \times 10^{-19} \text{ m}^2$	Wang and Small (2014)
Porosity of the caprock and seal bottom (ϕ_{cap} and ϕ_{seal})	0.05	Wang and Small (2014)
Salinity	67 g/l	Estimated
P-wave velocity of the caprock and seal bottom ($V_{\rm cap}$ and $V_{\rm seal}$)	3500 m/s	Mavko et al. (2009)
P-wave velocity of $CO_2(V_n)$	292.9 m/s	NIST
Initial datum pressure (P_0)	14.76 MPa	Erlström et al. (2011)
Initial average brine density (ρ_w)	1052 kg/m^3	Duan et al. (2008)
Initial average brine viscosity (μ_w)	$4.2 \times 10^{-4} \text{ Pa s}$	Span and Wagner (1996)
Average isothermal compressibility of brine (c_w)	$3.8 \times 10^{-10} \text{ 1/Pa}$	Duan et al. (2008)
Average CO_2 density (ρ_n)	520 kg/m^3	Span and Wagner (1996)
Average isothermal compressibility of CO_2 (c_n)	$9 \times 10^{-8} \text{ 1/Pa}$	Span and Wagner (1996)
Average CO_2 viscosity (μ_n)	$3.9 \times 10^{-5} \text{ Pa s}$	Fenghour et al. (1998)
Bulk modulus of dry frame rock (G_{dry})	$3 \times 10^{9} \text{ Pa}$	Caspari et al. (2011)
Bulk modulus of rock matrix (G_m)	$3.7 \times 10^{10} \text{ Pa}$	Mavko et al. (2009)
Shear modulus of saturated rock (N_{sat})	$2.5 \times 10^{10} \text{ Pa}$	Mavko et al. (2009)

where the values of the reference permeability $k_{\rm ref}$, porosity $\phi_{\rm ref}$, and entry pressure $P_{d,\rm ref}$ are 1×10^{-13} m², 0.25, and 8700 Pa, respectively (Rasmusson et al., 2014). In the scenario 2layers_B, the values of the model parameters are switched between the layers.

More realistic values of the aforementioned flow and elastic model parameters can be estimated by laboratory experiments on core samples taken from the storage site.

Relationship between flow properties and fluid saturation.—

The initial single-phase hydraulic conductivity K_w and specific storage S_{sw} of the aquifer are related to the intrinsic permeability k, porosity ϕ , brine density ρ_w , and viscosity μ_w in equations 3 and 4

$$K_{w} = \rho_{w} g\left(\frac{k}{\mu_{w}}\right),\tag{3}$$

$$S_{sw} = \rho_w g(\phi c_w), \tag{4}$$

where ρ_w , μ_w , and c_w are assumed constant by averaging the values within the reservoir. In equation 4, the rock compressibility is neglected because the value of a sandstone is usually one to two orders of magnitude smaller than that of CO_2 given the pressure and temperature conditions in this study (Vilarrasa, 2012). Furthermore, hydraulic diffusivity of the initial CO_2 -free formation D_{pre} is defined as the ratio between K_w and S_{sw}

$$D_{\text{pre}} = \frac{k}{\phi c_w \mu_w}.$$
 (5)

The transferred values of D_{pre} for the three scenarios are listed in Table 2

After CO_2 injection, considering CO_2 and brine as a phase mixture, the mixed-phase diffusivity D_{post} is determined by the intrinsic permeability and porosity, the fluid properties of brine and CO_2 (density, viscosity, and compressibility), the relative permeability, and the saturation of the two phases (Hu et al., 2016)

$$D_{\text{post}} = \frac{K}{S_s} = \left(\frac{k}{\phi}\right) \left[\frac{\frac{k_{rw}}{\mu_w} \rho_w + \frac{k_{rn}}{\mu_n} \rho_n}{(S_w c_w + S_n c_n)(S_w \rho_w + S_n \rho_n)} \right], \quad (6)$$

where k_{rw} and k_{rn} are the relative permeability of brine and CO_2 , respectively. Equations 5 and 6 indicate that the diffusivity varies with CO_2 saturation. Figure 3 displays three different $D - S_n$ models for the three scenarios. Model 1 (black solid line) is for the homogeneous scenario. Models 2 (red solid line) and 3 (blue solid line) are for the scenarios 2layers_A and 2layers_B, relating to the

two layers. Model 2 is for the low-permeability layer, and model 3 is for the high-permeability layer (Figure 2 and Table 2). For all models, diffusivity is smaller than that prior to CO_2 injection, which provides a basis for the inversion of diffusivity changes. However, it is also noticeable that, due to the nonmonotonic $D_{\rm post} - S_n$ relationship, one diffusivity value could correspond to two different saturation values, except when the CO_2 saturation is very low $(S_n < 0.05-0.1)$. This could introduce uncertainties for estimating of CO_2 saturation directly from diffusivity.

Relationship between the P-wave velocity and fluid saturation.-To infer CO₂ saturations and their temporal or lateral variation from seismic-velocity tomograms or to calculate the change in seismic velocity due to a change in CO₂ saturation, a specific relationship between velocity and CO₂ saturation needs to be assumed. Usually, such a relationship is determined by laboratory tests of field samples (Vanorio et al., 2011). In this study, we apply the Gassmann-Wood theory (Wood, 1941; Gassmann, 1951), which is valid at low seismic frequencies, to characterize seismic velocity in a rock that is saturated with a fluid mixture (Caspari et al., 2011). The Gassmann-Wood rock-physics model was chosen as one possibility out of the several realistic theories for different CO₂ patch sizes and local CO₂ distribution. Although the choice of rock-physics model and its calibration is critical for field studies to get a realistic estimation of CO2 saturation, the choice of rock-physics model is somewhat arbitrary for synthetic studies. The parameters used

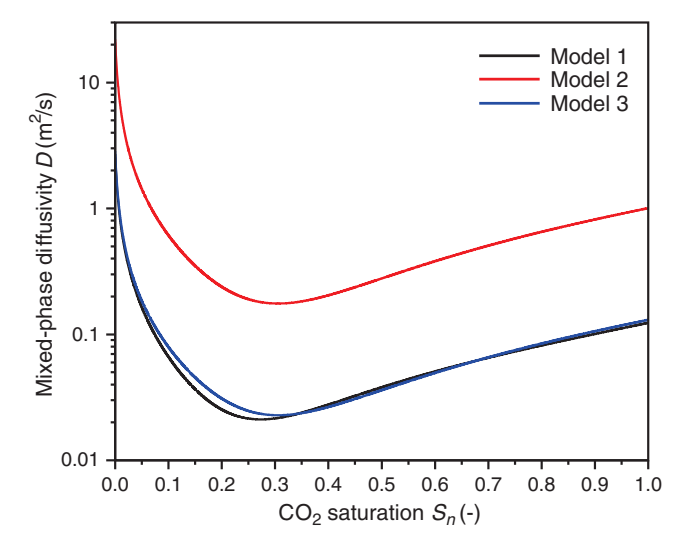


Figure 3. Diffusivity D versus CO_2 saturation S_n . Model 1: homogeneous scenario; model 2: layer with small permeability, k; and model 3: layer with large k.

Table 2. Parameter values of the reservoir in the three scenarios. Hydraulic conductivity, specific storage, diffusivity, entry pressure, and velocity are calculated based on the intrinsic permeability and porosity.

Scenario	Zone	k (m ²)	φ (-)	K_w (m/s)	S_{sw} (1/m)	$D \text{ (m}^2/\text{s)}$	P_d (Pa)	V (m/s)	c_p (J/kgK)	$\kappa_{\rm wet} \ ({ m W/mK})$	$\kappa_{\rm dry}~({ m W/mK})$
Homogeneous	1	1×10^{-13}	0.23	2.46×10^{-6}	9.1×10^{-7}	2.7	4000	4465	930	3	4.5
2layers_A	1 2			2.46×10^{-5} 2.46×10^{-6}		22.36 2.86	2932 8143	4579 4454	860	2.5	4.5
2layers_B	1	1×10^{-13}	0.22	2.46×10^{-6}	8.6×10^{-7}	2.86	8143	4454			
	2	1×10^{-12}	0.28	2.46×10^{-5}	1.1×10^{-6}	22.36	2932	4579			

ID6 Hu et al.

for the calculation of the velocities are given in Table 1, and for the equations used, see Appendix B.

The initial velocity of the storage formation (Table 2) is calculated based on equation B-4 by assuming a CO_2 -free reservoir $(S_n = 0)$. The velocity difference ΔV is defined as the difference between the velocity before (V_{pre}) and after (V_{post}) CO_2 injection

$$\Delta V = V_{\text{post}} - V_{\text{pre}}.\tag{7}$$

Analogs to the relationship of $D-S_n$ (Figure 3), $\Delta V-S_n$ is plotted in Figure 4 for five different models (see above). Similar to $D-S_n$, the relationship between ΔV and S_n is also not monotonic. Slight differences among these models are because of the different porosities for each of them. For all models, initial velocity declines due to the CO_2 injection. The ΔV decreases steeply along with the increased S_n because S_n is smaller than 0.15–0.25. When S_n is larger than 0.15–0.25, ΔV increases gently along with S_n . The maximum and minimal velocity changes are shown in models 2 and 3, with the value of approximately -350 and -200 m/s, respectively. However, changes of V along with S_n are obviously smaller than those of D.

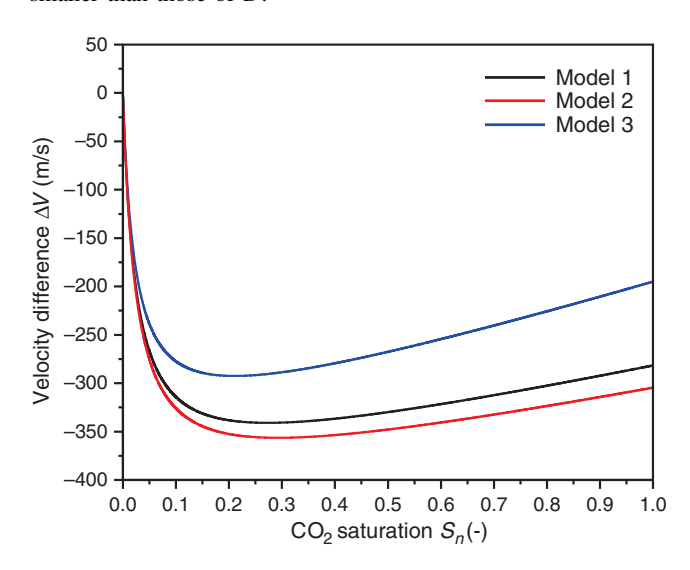


Figure 4. Velocity difference ΔV versus CO_2 saturation S_n . Model 1: homogeneous scenario; model 2: layer with small k; and model 3: layer with large k.

Table 3. Fluid-injection rate and duration of the test sequence

Scenario	Time	Q_c (stage 2)	Q_c (stage 4)	$T_{\rm inj}$	$T_{\rm rec}$	T_{S1}	T_{S2}	T_{S3}	T_{S4}	T_{S5}
		(kg				(h)				
Homogeneous	Short	0.01	0.02	120	240	4	4	4	4	4
	Long			360	240	6	6	6	6	6
2layers_A	Short	0.01	0.01	120	40	0.7	0.7	0.7	0.4	0.4
	Long			320	110	1.1	1.1	1.1	0.7	0.7
2layers_B	Short	0.015	0.01	90	40	0.4	0.4	0.4	0.7	0.7
	Long			230	60	0.8	0.8	0.8	1.1	1.1

Forward simulation

Single-phase and two-phase flow simulation

An open source code, PFLOTRAN (Hammond et al., 2014), is used for the forward simulation of the single-phase and two-phase flow processes. For the forward simulation, we focus on the early-stage injection procedure. Residual trapping, chemical reactions with the rock matrix, and any geomechanical processes are neglected. The entire simulation is divided into four stages: baseline study (stage 1), CO₂ sequestration (stage 2), shut-in period (stage 3), and repetition of interference fluid injection tests (stage 4).

Stage 1: Baseline study.—At this stage, brine is injected from the bottom to the top sources in the borehole. For all three scenarios, each injection lasts for 2 h following a recovery period of 15 h, allowing the pressures to fall back to the initial hydrostatic condition. Pressure transients during the injections are used for depicting the structure of the aquifer, as well as the initial hydraulic conductivity and specific storage.

Stage 2: CO₂ sequestration.—At this stage, for each scenario, CO₂ is injected in a depth-integrated way, that is, at the injection well, it is injected over the entire aquifer. Injection durations are different (Table 3) to generate two plumes of different size. We discriminate the two injections by naming them the "short injection" and the "long injection," respectively. The injection rate for the homogeneous scenario and 2layers_A is 0.01 kg/s, and for 2layers_B, it is 0.015 kg/s. The durations of the short and long injections for the three scenarios are listed in Table 3.

Stage 3: Shut-in period.—This stage is included for recovering the pressure to a quasisteady state. Durations are summarized in Table 3. In applications in practice, the experiments of the next stage can be prepared now.

Stage 4: Repetition of interference fluid injections (stage 1).—As soon as the pressure recovers to a quasisteady state, the CO₂ is injected sequentially comparably with previous brine injections. Pressure fluctuations are recorded at the observations for tomographic inversion. The injection rate for the homogeneous scenario, 2layers_A, and 2layers_B is 0.02, 0.01, and 0.01 kg/s, respectively. Durations of one injection and the following recovery period are set to be equivalent (Table 3).

Hydraulic traveltime calculation

The pressure transients at the observation well derived from stages 1 (baseline) and 4 (after $\rm CO_2$ sequestration) are used for calculating the hydraulic traveltimes, following the work of Brauchler et al. (2003) and Hu et al. (2015). For the continuous fluid injections, the hydraulic traveltime is determined by the first time derivative of the pressures. The time at which the maximum derivative appears at a receiver is defined as the peak time. However, here we use the early traveltime diagnostic for the inversion because it resolves the preferential flowpaths better than the late diagnostic. We use a 20% traveltime di-

agnostic (t - 20%) for the inversion as suggested by Hu et al. (2015), which refers to the time at which the pressure derivative rises to 20% of its peak amplitude. The diagnostic is then converted to "traveltime" \hat{t} as input for an eikonal solver based on the following equation:

$$\hat{t} = \sqrt{6t_{\alpha,d}} \times \sqrt{-W\left(\frac{\alpha_d^{2/3}}{e}\right)},\tag{8}$$

where $t_{\alpha,d}$ is t - 20% and W is Lambert's W function. Here, α_d is the pressure-derivative ratio term, representing the quotient of the temporal and spatial pressure derivative and the maximum pressure derivative. Note, that to compare with seismic traveltimes, the phrase "hydraulic traveltimes" hereafter refers to the converted term \hat{t} , and thus the unit is $s^{0.5}$. The hydraulic traveltimes are perturbed with 1% of Gaussian noise prior to the inversion, which is a realistic noise level for field studies (see, e.g., Ajo-Franklin et al., 2013).

Seismic-traveltime calculation

Based on the flow simulations discussed in the section "Single-phase and two-phase flow simulation," seismic traveltimes (i.e., the first arrival times of P-wave pulses) are calculated for stage 1 (baseline) and stage 4 (after CO_2 sequestration). The seismic velocity distribution for the different scenarios at the two stages is calculated using the equations discussed in Appendix B (equations B-1–B-4) and the parameters of Tables 1 and 2. The traveltimes are computed in the high-frequency limit using the finite-difference eikonal solver of Podvin and Lecomte (1991) on a mesh with 240×340 cells and a cell size of 0.25 m. Traveltimes between all 76 sources and 76 receivers are calculated, so that 5776 data points are available for each data set. Similar to the hydraulic traveltimes, all seismic traveltimes are also contaminated with 1% Gaussian noise before inversion.

Traveltime-based inversion

Inversion of hydraulic traveltimes

The inversion scheme of the hydraulic traveltimes is based on Brauchler et al. (2003). The hydraulic traveltime \hat{t} is related to the reciprocal value of the square root of hydraulic diffusivity \sqrt{D} by a line integral

$$\hat{t} = \int_{x_1}^{x_2} \frac{ds}{\sqrt{D(s)}}. (9)$$

A staggering technique is applied to the inversion procedure for improving the resolution of the final tomogram, and to weaken the effect of positioning (Vesnaver and Böhm, 2000; Somogyvári et al., 2016). The base model used for the inversion is discretized by five columns and four rows. By shifting the underlying model nine times in the horizontal direction and three times in the vertical direction during the inversion, the final tomogram reaches a resolution of 50×16 cells.

Repetition of the inversion to the time-lapse data sets delineates the diffusivity distribution at different times. For removing the influence of the preinjection structure, we define the diffusivity difference ΔD as follows:

$$\Delta D = \log_{10} D_{\text{post}} - \log_{10} D_{\text{pre}}$$

$$= \log_{10} \left[\frac{c_w \mu_w (k_{rw} \rho_w / \mu_w + k_{rn} \rho_n / \mu_n)}{(S_w c_w + S_n c_n) (S_w \rho_w + S_n \rho_n)} \right]. \tag{10}$$

Note, the unit of ΔD is nondimensional because the right side of equation 10 can be formulated as $\log_{10}(D_{\mathrm{post}}/D_{\mathrm{pre}})$, which can be considered as the logarithm of the normalized diffusivity. By assuming the state variables (the density, viscosity, and compressibility) of the brine and CO_2 are constant, equation 10 shows that the ΔD is merely determined by the fluid saturation and the pore-size distribution λ . In the supporting information, Supplemental Figure S1 presents the change of ΔD along with the CO_2 saturation S_n . The model of the homogeneous scenario shows a slight difference from the other two models due to their varying λ values (model for the homogeneous scenario: $\lambda = 0.76$; the other two models: $\lambda = 1.5$).

Inversion of seismic traveltimes

The seismic traveltime data sets that are simulated for the different scenarios and at the different times (stage 1 and stage 4) are inverted using the algorithm of Doetsch et al. (2010b). It implements an Occam's type inversion with stochastic regularization (chosen integral scales of $I_x = 16$ m, $I_z = 8$ m), in which the regularization strength is decreased until the data are fit to the error level. The assumed error on the traveltimes is 1%, in accordance with the noise contamination level, and all inversion results fit the data to that assumed error level.

The inversion results of the baseline inversion are used as starting and reference models for the time-lapse inversions of data acquired during the multilevel CO_2 injections. A difference inversion scheme is being used that inverts for the changes to the baseline inversion result (Doetsch et al., 2010a), so that even small changes to the baseline model can be resolved and inversion artifacts are minimal. The results of the time-lapse inversions are analyzed and shown as a change in velocity compared with the baseline inversion result.

Clustering and zonal calibration

Time-lapse 1D and 2D clustering

The goals of clustering are to determine the baseline structure and to delineate the extent of CO_2 plumes at different times. The unlabeled data of inverted tomograms are partitioned into homogeneous groups, in which the hydraulic conductivity and specific storage are constant. We first apply individual clustering (i.e., 1D clustering) to the diffusivity tomograms of the CO_2 -free aquifer. Spatial heterogeneity is determined by the clusters that are used in the following calibration. Individual and JT (i.e., 2D clustering) are used for the tomograms of the diffusivity difference and velocity difference obtained after CO_2 injection. Compared with individual clustering of PT or ST, we hereafter refer to joint clustering as "JT."

The clustering approach is a modified k-means method. Unlike the usual k-means method (MacQueen, 1967), the centroids of the clusters are determined by fitting the data histogram with the summation of multiple 1D or 2D Gaussian functions. The 1D and 2D clusterings are performed in a time-lapse strategy. The centroids are determined by the data histogram at long injection, and then they are applied at short injection as well. The inverted shapes are compared with the true plumes and their ambient aquifers by analyzing the dissimilarity in their shape. Three metrics can be used for obtaining this goal: over-

ID8 Hu et al.

estimation rate, underestimation rate, and total pixel misclassification error rate. These metrics can loosely depict the dissimilarity of two binary images, which in our study are the true plume and inverted plume. They are detection performance measures, regardless of the pixel positions and intensity. Definitions of these metrics are given in the following (Baddeley, 1992).

Let A, B, and X be the true plume, inverted plume, and the pixel raster (i.e., the entire inversion model), respectively. Pixels that belong to B but not A are called type I errors; pixels that belong to A but not B are called type II errors.

Type I errors (α), also called the "overestimation rate," are calculated by

$$\alpha(A,B) = \frac{n(B \setminus A)}{n(X \setminus A)}.$$
 (11)

Type II errors (β) , or the underestimation rate, are calculated by

$$\beta(A,B) = \frac{n(A \setminus B)}{n(A)},\tag{12}$$

where n(A) and n(B) are the number of pixels in the true plume A and inverted plume B. Here, n(X) is the total number of pixels in the raster. Based on these two error rates, the total pixel misclassification error rate (ε) for binary images is defined as

$$\varepsilon(A,B) = \frac{n(A\Delta B)}{n(X)} = \alpha(1-r) + \beta r. \tag{13}$$

Zonal calibration and estimation of saturation

Calibration of CO₂ saturation in a multiple-process-coupled forward simulator usually is computationally demanding. In our study, one run of the 2D two-phase flow model in PFLOTRAN costs 1 h to several days depending on the model heterogeneity (data are based on a workstation, 32× Xeon 3.1 GHz, 64 GB RAM). For reducing the model complexity and accelerating calibration, we use MODFLOW (Harbaugh, 2005) to run the forward simulation during the inversion procedure, considering CO₂ and brine as a mixed phase. Compared with PFLOTRAN, one run of the mixed-phase flow model merely

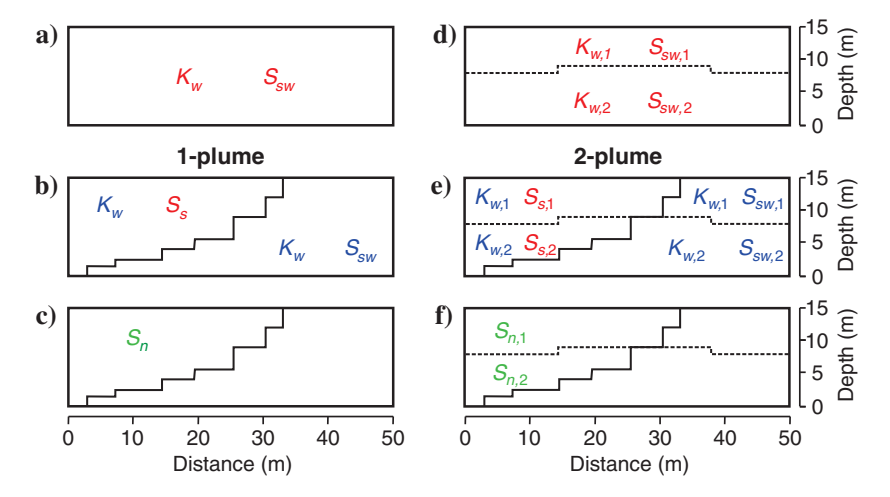


Figure 5. Conceptual scheme for zonal calibration. Parameters in red are calibrated, and those in blue are fixed during the calibration. Parameters in green are converted by the specific storage-saturation models.

costs 2–4 min (data are based on a PC, Intel i7-3370S 3.1 GHz, 16 GB RAM). This greatly reduces the computing time and thus improves the calibration efficiency. Figure 5 presents a summary of two different zonal calibration steps carried out sequentially.

First, for the preinjection, we merely calibrate the effective hydraulic conductivity and specific storage assuming that the aquifer is homogeneous (Figure 5a). The calibrated values of K_w and S_{sw} are assigned to the clustered aquifer zone for the postinjection (Figure 5b). As pointed out in Hu et al. (2015), the mixed-phase conductivity K of the plume zone shows only minor changes during CO_2 injection, and thus this value is kept the same as K_w for the postinjection. Only the mean mixed-phase specific storage S_s of the plume zone needs to be calibrated (Figure 5b). The mean S_n of the plume is then transferred from S_s (Figure 5c) by the following equation:

$$S_{s} = \phi g(\rho_{w} S_{w} + \rho_{n} S_{n})(c_{w} S_{w} + c_{n} S_{n}). \tag{14}$$

Second, the calibration is conducted considering the heterogeneity of the reservoir. For the two layered scenarios, the aquifer structure is determined by clustering the inverted $D_{\rm pre}$, and the K_w and S_{sw} of each cluster are calibrated primarily for the preinjection (Figure 5d). For the postinjection, the plume zone can be divided into two secondary plumes based on the aquifer structure. The functions K_w and S_{sw} of each cluster in the aquifer zone are fixed, as well as K in the plume zone ($K = K_w$) (Figure 5e). The mixed-phase specific storage S_s of the two secondary plumes is calibrated and converted to the S_n of the two plumes in equation 14.

To reduce the potential nonuniqueness of the calibration results in the second step, the acquired values of S_n in the first step are used as prior information for the following calibration. Here, we make an assumption that the S_n in the high-permeability layer is larger than the low-permeability layer. The mean S_n (Figure 5c) is transferred back to the two S_s values for the layered structure, considering the porosities are different for the two layers. These two values are used for constraining the calibration. For instance, presuming $K_{w,1}$ is larger than $K_{w,2}$ in Figure 5d, parameters S_s of the two layers transferred by the mean S_n are expressed as $\bar{S}_{s,1}$ and $\bar{S}_{s,2}$, respectively. Then, the calibrated $S_{s,1}$ should be larger than $\bar{S}_{s,1}$, and $S_{s,2}$ is smaller than $\bar{S}_{s,2}$. The validity of this assumption depends on

whether the initial aquifer structure can be identified properly.

Figure 6 shows five different models for converting S_s back to S_n . Models 1, 4, and 5 (black solid line and green and pink dashed lines) show the relationship between the effective S_s and S_n for a one-plume structure in three different scenarios. Models 2 and 3 (blue and red solid lines) are used for obtaining the saturation within each secondary plume for the two layered scenarios.

The performance of the calibration is evaluated by calculating the saturation error ξ . It is estimated by the difference between the calculated saturation ($S_n^{\rm cal}$) and the arithmetic mean of the true saturations within the same inverted plume or secondary plume structure (note, not the true plume extent) normalized by $S_n^{\rm true}$

$$\xi(\%) = \frac{S_n^{\text{cal}} - S_n^{\text{true}}}{S_n^{\text{true}}} \times 100.$$
 (15)

RESULTS

The procedure described above is tested step by step on the three reservoir scenarios to compare the performance of PT and ST.

PT and ST traveltimes

For eliminating the effect of different source-receiver configurations for PT and ST, we only compare the traveltimes of the tomographic arrays in the horizontal direction. Note that the seismic inversion is based on the full data set of the traveltimes (i.e., the total 5776 traveltimes). Supplemental Table S1 (see the supporting information) lists the statistics of these traveltimes (noise-free and with noise) in the horizontal direction derived for PT and ST. The horizontal hydraulic traveltimes vary from 12.7 (in scenario 2layers_B) to 173.4 s^{0.5} (in the homogeneous scenario). The hydraulic traveltimes increase by 154%–486% after CO₂ injection. The most effected horizontal seismic traveltimes through the reservoir increase from 11.2 ms before CO₂ injection to 11.76 ms after injection, corresponding to an increase of 5%. Overall, changes of the seismic traveltimes are much smaller than for hydraulic traveltimes, with changes ranging from 0% to 5%.

To compare the results for PT and ST, the relative spread of the horizontal traveltimes (i.e., the standard derivation normalized by the mean) is examined (see Supplemental Table S1). At preinjection, the relative spread of the noise-free traveltimes in the homogeneous scenario is zero. For the traveltimes with noise, the relative spread is consistent with the noise level (1%). In the two layered scenarios, the relative spread at preinjection of the hydraulic traveltimes (0.23 for 2layers_A and 0.1 for 2layers_B) is much greater than the seismic traveltimes (approximately 0.01–0.02). At postinjection, the relative spread for the seismic traveltimes is approximately 0.01–0.02 for all three scenarios, whereas for the hydraulic traveltimes, it reaches from 0.1 to 0.7. In the following, we only present and discuss the results derived from the data with noise, thus considering the more realistic cases.

Diffusivity and velocity tomograms

The results obtained from two-phase flow simulation for the different scenarios are considered as the "truth," and these serve as a reference for assessing tomographic inversion. The values of true diffusivity, velocity, and their differences for pre-, short, and long injections are calculated based on the simulated true CO₂ saturation, according to equations 3–7 and 10. The true profiles and inverted tomograms are depicted in Figure 7, and a complete list can be found in the supporting information (Supplemental Tables S2 and S3).

In the homogeneous scenario, the true D and V at preinjection are 2.7 m²/s and 4465 m/s, respectively (Figure 7I-a and 7I-g). The inverted D varies from 2.8 to 3 m²/s (Figure 7I-d), which is slightly different to previous results by Hu et al. (2015) for the same scenario due to the noise for hydraulic traveltimes that is included here. The seismic tomography includes the caprock above and below the reservoir, and the reservoir can be clearly identified in the tomograms (see Figure C-1). Inside the reservoir, the inverted values of V range from 4064 to 4755 m/s (Figure 7I-j). The relative spread is greater than that observed for the inverted D. The inverted velocity in caprock/bottom seal is much less than the reservoir, which varies from 3413 to 3800 m/s. In the scenarios 2layers_A and 2layers_B, the true D and V of the initial CO_2 -free formation are 22.4 m²/s and 4579 m/s for the high-permeability layer, and 2.9 m²/s and 4454 m/s for the low-

permeability layer (Figure 7II-a, 7II-g, 7III-a, and 7III-g). The inverted D for 2layers_A and 2layers_B is within a range smaller than the true values (3.6–10.2 m²/s for 2layers_A and 7.2–12.2m²/s for 2layers_B, Figure 7II-d and 7III-d). The inverted V shows a similar range for the two scenarios, which is 3998–4930 m/s and 4067–4854 m/s, respectively (Figure 7II-j and 7III-j).

For the two postinjection periods, both of the true D and V follow a nonmonotonic change along with S_n (Figures 3 and 4). The true D decreases by up to two orders of magnitude, resulting in a minimum ΔD (i.e., the difference of logarithm D at pre- and postinjection) value of approximately -2 for all three scenarios (Figure 7I-b, 7I-c, 7II-b, 7II-c, 7III-b, and 7III-c). The minimum ΔV is -340.9 m/s for the homogeneous scenario, and it is -356.4 m/s for 2layers_A and 2layers_B. It is noticeable that for each scenario, the minimum ΔD and ΔV are the same during the short and long injection because they do not correspond to the maximum S_n value (Supplemental Figure S1 and Figure 4). Likewise, in the true profiles of the flow and seismic parameters, the smallest values are shown within the plume, where S_n has a moderate value. The inverted ΔD for the homogeneous scenario and 2layers_A span a smaller range compared with the truth (Figure 7I-e, 7I-f, 7II-e, and 7II-f). In contrast, the inverted ΔD has a larger range than the truth for 2layers_B (Figure 7III-e and 7III-f). In general, the absolute values of the inverted ΔV are smaller than the true values for all the three scenarios.

1D and 2D clustering structure

Prior to the zonal calibration, clustering was implemented based on the inverted results to obtain the plume shape at different times. First, according to the inversion performance of the baseline, the inverted D derived prior to CO_2 injection was clustered to determine the structure of the reservoir. Subsequently, the inverted ΔD and ΔV were clustered individually (1D clustering), and then jointly (2D clustering). To judge the different approaches, the plume shapes derived from 1D and 2D clustering processes were compared with the true plumes according to the three aforementioned metrics (overestimation rate, underestimation rate, and total misclassification rate, calculated in equations 11-13). Figure 8 depicts the clustering

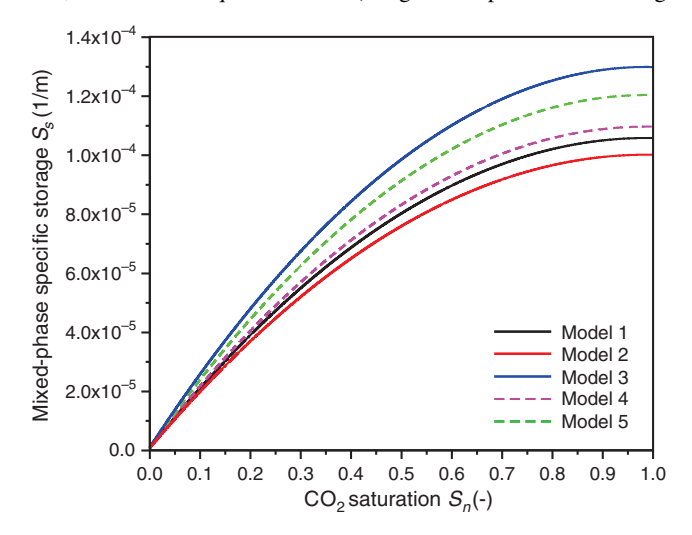


Figure 6. Mixed-phase specific storage S_s versus CO_2 saturation S_n . Model 1: homogeneous scenario; model 2: layer with small k; model 3: layer with large k; model 4: integrated model for 2layers_A; and model 5: integrated model for 2layers_B.

ID10 Hu et al.

results, with the metrics shown as the numbers in the same figure. In terms of misclassification, ST outperforms the PT and JT (i.e., joint clustering), but the numbers are generally similar.

Zonal calibration and calculated saturations

Based on the identified aquifer and plume zones by 1D and 2D clustering, zonal calibration was conducted. The effective K_w and

 S_{sw} of the original formation (ignoring its heterogeneity) were calibrated primarily in MODFLOW with PEST (Doherty, 2010), using the pressure observations derived from the full model. Because of the proxy, the calibrated K_w and S_{sw} at preinjection are slightly smaller than the true values (the errors are approximately 10%). The calibrated K_w and S_{sw} were then used as the prior information for the aquifer zone, and the calibrated K_w for the plume zone was also fixed for the postcalibration. The calibrated S_s of the plume zone (see

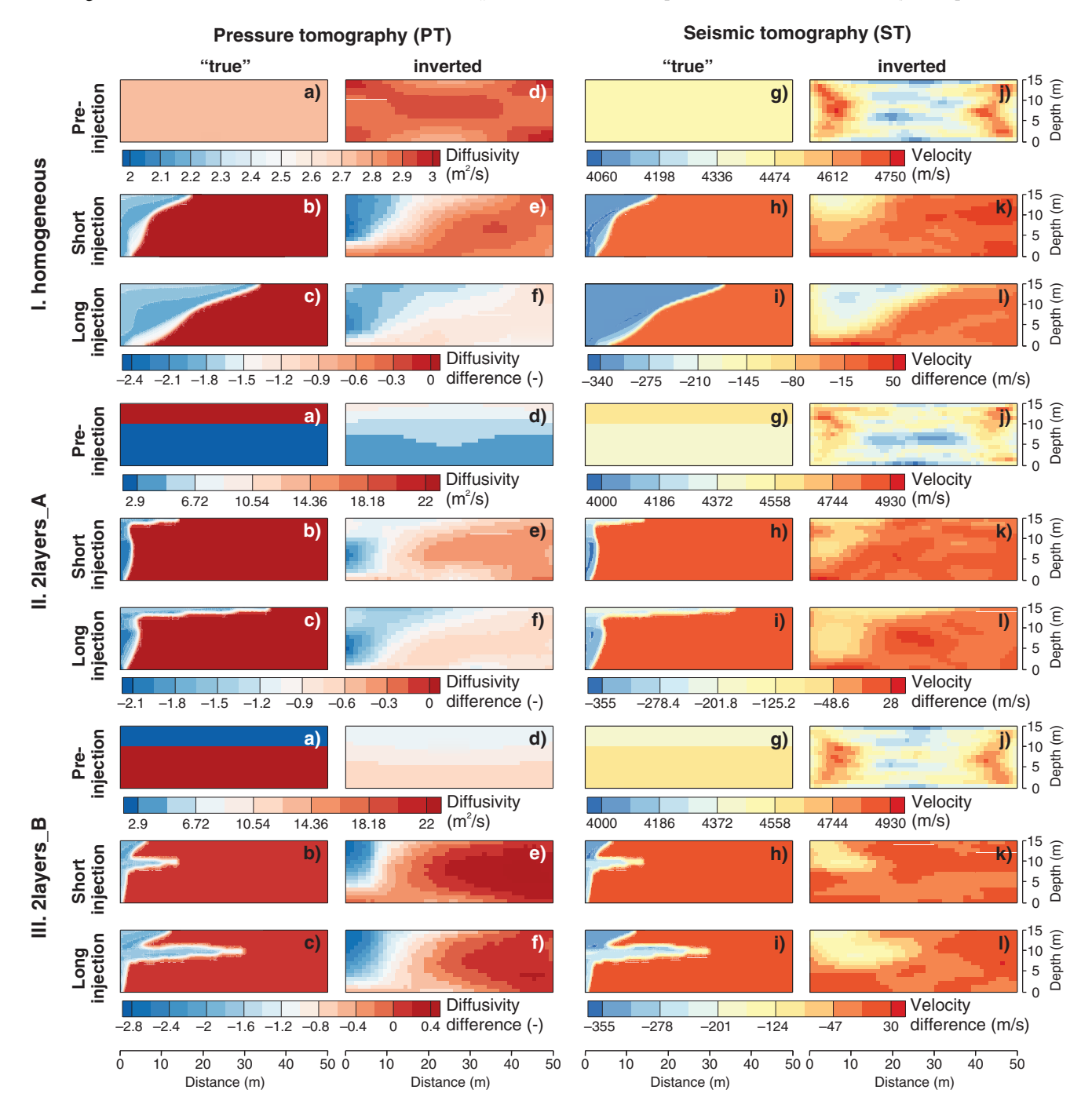


Figure 7. True profiles versus inverted tomograms in the three scenarios (the true profiles are on the left, and the inverted tomograms are on the right). For ST, the model extends 30 m above and below the reservoir (see Figure C-1) to include the caprock and bottom seal (V = 3500 m/s). CO₂ is injected at the left of the model, and the migrating plume can be seen in PT and ST by the inverted tomograms. The internal structure of the aquifer can only be resolved using PT because internal variations in seismic velocity are too small compared with the contrast to caprock.

the supporting information, Supplemental Table S5) was then converted to S_n in the homogeneous scenario, as well as 2layers_A and 2layers_B by models 1–3 (Figure 6), respectively. The calibration results of the 1- and 2-plume structures for the three scenarios are presented in Figure 9 and Supplemental Figure S3 and Supplemental Tables S4 and S6, respectively.

Calibration quality was evaluated by calculating the error of S_n (ξ) using equation 15 (see Supplemental Table S5). For 1-plume structure, in the homogeneous scenario, ξ varies from -3% to 11% except for the short injection, case in which the plume structure was derived from ST (ξ is 89%). In scenario 2layers_A, ξ ranges from 36% to 51% for short injection, which is generally higher than for long injection (23%–29%). In scenario 2layers_B, ξ remains low (<10%) except for the case of PT for the long injection (46%). Overall, the JT results are not always the best, but they are robust. The estimation errors are reduced, maintaining errors at less than 36% for all

the scenarios. For the 2-plume structure, ξ changes from -24% to 127% in 2layers_A, and which varies from 0% to 63% in 2layers_B (see Supplemental Table S6).

DISCUSSION

PT and ST traveltimes

Changes in PT and ST traveltimes are a direct measure of the sensitivity to relevant changes in the reservoir. Our results indicate that variability of hydraulic traveltimes is generally much larger than seismic traveltimes. A great variability of traveltimes is favorable because this potentially allows for better resolution of the subsurface. Through the comparison of relative spread in three scenarios, it is implied that relative spread correlates with the degree of heterogeneity. No relative spread indicates noise-free homogeneous conditions. Prior

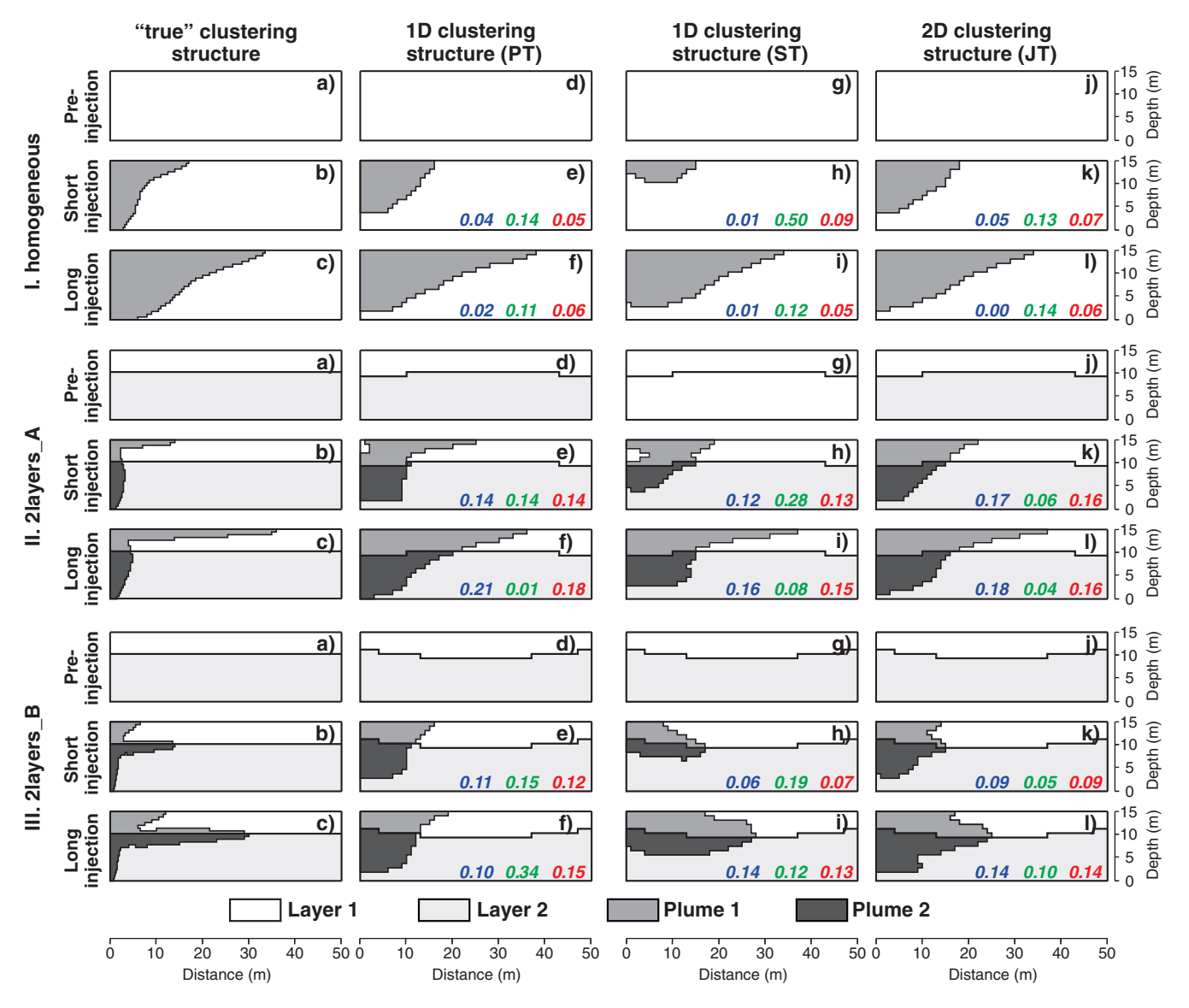


Figure 8. True clustering structures (subgraphs a-c) versus 1D (subgraphs d-i) and 2D (subgraphs j-l) clustering structures in the three scenarios. Numbers in blue: overestimation rate (α); numbers in green: underestimation rate (β); and numbers in red: total misclassification rate (ϵ). The performance among PT, ST, and JT is comparable in the homogeneous scenario and 2layers_A, whereas in 2layers_B, JT shows a combination of the 1D clustering results from PT and ST.

ID12 Hu et al.

to CO₂ injection, the highest relative spread is obtained for 2layers_A, in which small-scale contrasts in permeability are simulated by a relatively thin conductive layer. After CO₂ injection, the highest relative spread is in 2layers_B, indicating the largest contrasts in permeability between the relatively thick conductive layer and the CO₂ plume. In addition, it is remarkable that the imposed noise has a small impact on the relative spread of the hydraulic traveltimes because the spread of the noise-free data is much larger than the noise level.

Diffusivity and velocity tomograms

In Figure 7, two-phase simulations show that the fronts of the plumes in the two heterogeneous scenarios have more complicated geometries (Figure 7II-b, 7II-c, 7III-b, and 7III-c) in comparison with the true plumes in the homogeneous scenario (Figure 7I-b and 7I-c). The high-permeability layer largely controls the plume. The CO₂ migrates preferentially within the highly conductive layer, whereas the migration is also controlled by buoyancy, complicating the plume geometry. In 2layers_A, the plume distribution is representative for a multilayer system (i.e., two or more continuous layers) in which the top layer has the highest permeability. Here, the plume ultimately assembles at the top of the reservoir, which is caused by a combined effect of the high permeability of the upper layer and buoyancy (Figure 7II-b and 7II-c). However, the less permeable lower layer hinders expansion of the plume. The scenario 2layers_B exemplifies conditions in which a highly conductive channel exists between the

wells. Here, the plume travels faster at the bottom layer, forming a striking finger-like shape at the boundary of the two layers (Figure 7III-b and 7III-c). The finger is not delimited strictly below the boundary because of buoyancy effects.

At preinjection, the small range of inverted D still nicely reflects the homogeneous properties of the aquifer in homogeneous scenario. The strong velocity variation (3500 versus approximately 4500 m/s) between caprock/bottom seal and reservoir enables identification of the reservoir, but makes it difficult to judge if the reservoir itself is homogeneous or heterogeneous. In the two layered scenarios, the inverted D generally has a higher value and less data spread in 2layers_B, which, in this scenario, is due to the larger high-permeability area and also to shorter traveltimes. In addition, the inverted D tomograms in the two scenarios display a layered distribution, which is consistent with the true aquifer structure to some extent. However, the "perfectly" horizontal boundary between the two layers was not accurately reconstructed due to nonhorizontal tomographic rays as well as regularization, which both causes smearing between the inversion cells. Comparison of the three scenarios indicates that PT resolves the internal structure and especially the hydraulic properties of the aguifer better because it is related to permeability and porosity (equations 3–5). Usually, permeability shows much larger spatial variability than porosity. In contrast, ST is able to delineate the structure of the reservoir, but it fails to identify additional variations within the reservoir. Seismic velocity mainly depends on the

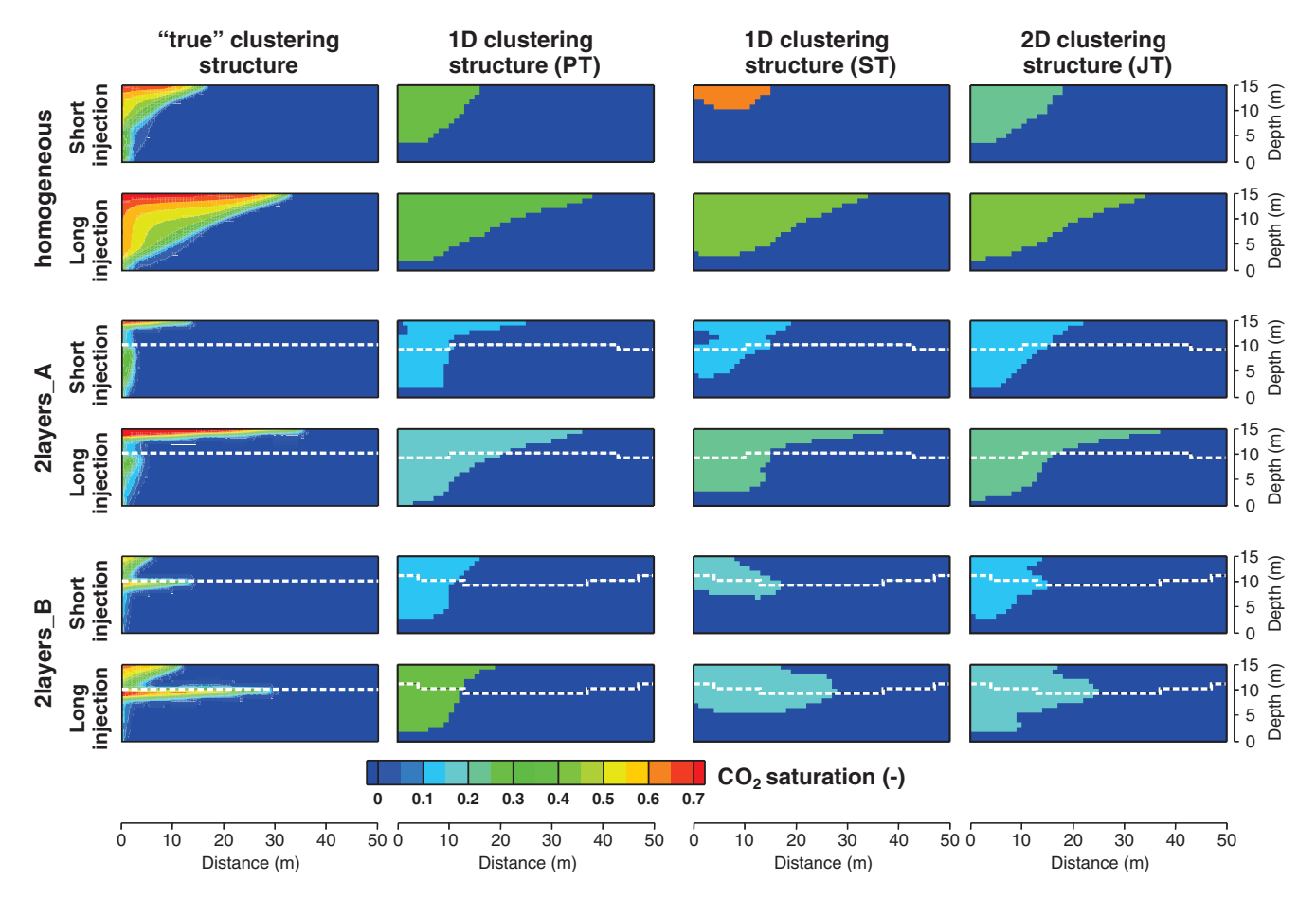


Figure 9. True versus calibrated saturations of three scenarios. The dotted white line indicates the boundary of two true or inverted layer boundaries. Calibrated CO₂ plume saturations are assumed to be homogeneous for each calibration and thus represent an average value within the plume.

porosity and rock density, which might only have slight variations within an aquifer. Velocity variations within the reservoir are only approximately 120 m/s prior to CO_2 injection, which is difficult to recover simultaneously with the 1000 m/s variation between reservoir and caprock/bottom seal.

At postinjection, the true profiles show that the contrast of ΔV caused by CO_2 is much smaller compared with ΔD . Inversion results of ΔD and ΔV are not consistent with the true values. Nevertheless, the information about the plume can still be inferred by the small values in the ΔD and ΔV tomograms. The ΔD tomograms of the two layered scenarios indicate that the variability of permeability has an adverse impact because PT is applied to the postinjection. The PT resolves the secondary plume in the lower permeability layer better. In the case that the contrast of diffusivity is sufficiently large at preinjection, the secondary plume in a higher permeability layer can still be identified (e.g., in 2layers_A, Figure 7II-e and 7II-f). Conversely, in 2layers_B, the finger at the layer boundary is masked in the ΔD tomograms (Figure 7III-e and 7III-f). This is mainly because the variations of the inverted D at preinjection are comparably small. The ST can capture the main front of the plume from the ΔV tomograms of all the scenarios because it is not influenced by the permeability. However, the lower relative spread of the seismic traveltimes limits the capability of ST to identify the small-size plumes in the low-permeability layer (Figure 7III-k and 7III-l).

Overall, the inverted values from the three scenarios at pre- and postinjection indicate that neither diffusivity nor velocity values can be precisely reproduced by the inversions. Direct transformation of inverted values to CO_2 saturation leads to an incorrect estimation. There are several reasons that can explain this. First, for PT and ST, the loose density of the trajectories or rays in the low-diffusivity or velocity parts can cause a nonuniqueness of the inversion solution in the tomograms. Second, these errors can also be attributed to inaccuracies introduced by using the single-phase proxy. Besides, the nonmonotonic relationship between the diffusivity or velocity and CO_2 saturation hampers deriving an exact CO_2 saturation value directly from the inverted diffusivity or velocity.

1D and 2D clustering structure

In the homogeneous and 2layers_A scenarios, clustering of D before CO₂ injection shows a homogeneous and two-layer aquifer structure (Figure 8I-d and 8II-d). The clustering results after CO₂ injection from 1D and 2D clustering are of comparable quality. Because of the similar distribution of the inverted ΔD and ΔV , they show a strong correlation (see the supporting information, Supplemental Figure S2a). Even 2D clustering does not significantly improve the results. In some cases, the 1D clustering results based only on PT or ST are better than the 2D clustering results. For instance, if we compare the total misclassification rate (Figure 8, red numbers) to assess the quality of the results, in the homogeneous scenario, the clustering result based on PT at short injection provides the best agreement with the true plume (Figure 8I-e). On the contrary, the clustering result from ST (Figure 8I-h) is the worst; thus, it has a negative impact on the final JT result (Figure 8I-k). In addition, in 2layers_A, during the short injection, the clustered ΔD and ΔV display a discontinuous distribution near the injection location (Figure 8II-e and 8II-h), yet this continuity vanishes in the jointly clustered plume (Figure 8II-k).

In 2layers_B, the two-layer structure also can be indicated by the 1D clustering of *D* (Figure 8III-d). However, for the two postinjection

periods, the plumes show a significant difference from the 1D clustering results. The geometries of the plumes delineated by PT are more vertical (Figure 8III-e and 8III-f), whereas those derived from ST show a more lateral distribution (Figure 8III-h and 8III-i). The ΔD and ΔV show less correlation during the 2D clustering process (see the supporting information, Supplemental Figure S2b). The dissimilarities between ΔD and ΔV hamper the acquisition of the 2D centroids for clustering the time-lapse data sets. Therefore, we cluster ΔD and ΔV in another way. The 2D histogram was fitted by a model composed of multiple Gaussian functions (the aguifer zone) and a uniform distribution (the plume zone). The cutoff of the aquifer and plume zones was at the edge of the Gaussian functions, in which the values are equal to the mean value of the uniform distribution. This was applied for the short- and long-injection runs. Consequently, the 2D clustered structures are deemed to be a superposition of the plumes from PT and ST (Figure 8III-k and 8III-l), but in a more systematic way.

Clustering works best for the homogeneous scenario according to the total misclassification rate ε (smaller than 0.1 for all the three scenarios). The heterogeneous scenarios show a higher misclassification due to the additional complexity. Values of ε indicate that the clustering performance in 2layers_B (ε : 0.07–0.15) is better than 2layers_A (ε : 0.13–0.18). The overestimation rate α shows a similar trend as ε . The plume extents are most overestimated in 2layers_A compared with the other scenarios. The underestimation rate β of the plumes is relatively high as the true plumes near the injection well or if the plume fronts are not accurately characterized (e.g., Figure 8I-h and 8III-f). In general, JT reduces the underestimation of the plume extent (e.g., Figure 8I-k, 8III-k, 8III-k, and 8III-l).

Saturation errors

The underestimation rate β is considered the most crucial criterion to assess proper spatial classification. In Figure 10, the saturation error ξ is plotted with β . It is clearly shown that, for each scenario, the increased β generally provokes a higher saturation error. This is be-

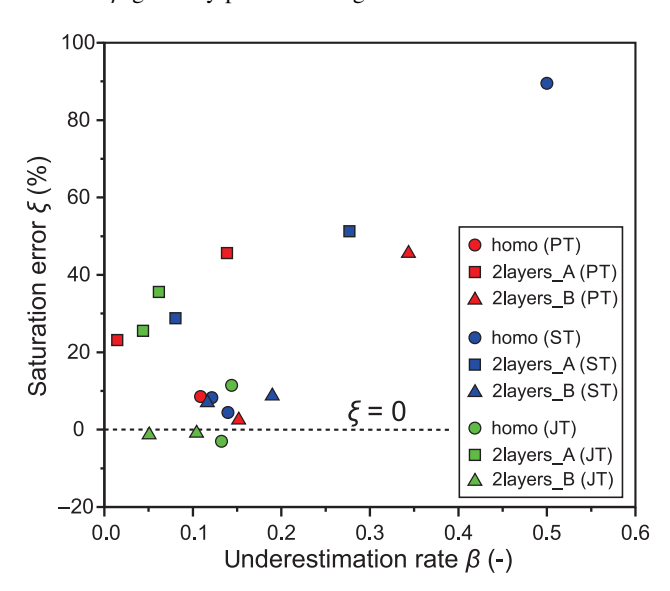


Figure 10. Underestimation rate β versus saturation errors ξ . The red and blue symbols are the calibrated results based on individual clustering structures derived from PT and ST, respectively. The green symbols represent the results derived by the JT. Each symbol exists twice, representing the short and long injection, respectively.

ID14 Hu et al.

cause the hydraulic conductivity and specific storage in the underestimated part of the plume are assigned the same values as the aquifer. As discussed in the section "Model parameters," the specific storage of a plume can be approximately 1–2 orders of magnitude larger than the ambient aquifer. Therefore, the underestimation of the plume size leads to a higher value of specific storage within the inverted plume.

In comparison with homogeneous and 2layers_B, 2layers_A shows higher estimation errors. This might be due to the overestimation of the plume extent. The true saturation S_n^{true} is derived by averaging the saturations within an inverted plume, that is, it is the arithmetic mean of these saturations. As S_s increases nonlinearly with S_n (Figure 6), the transferred S_n^{cal} might be different from the averaged S_n^{true} , even though they correspond to the same calibrated S_s .

For 2-plume structures in 2layers_A and 2layers_B, in general, the estimated S_n values are consistent with the fact that S_n is larger in the high-permeability layer. However, the estimation errors span a broader range in comparison with the previous results from the 1-plume structure. As discussed above, these errors can be due to the misclassification of the secondary plume in each layer. Moreover, they can also be attributed to the pressure discrepancy between the full model and the proxy. To obtain the specific storage of each secondary plume, more pressure measurements were used for the 2-plume structure than the 1-plume structure, and thus the calibration involved more pressure errors. This can be improved in future work by quantifying the errors between the two-phase forward simulation and the single-phase proxy under different conditions.

CONCLUSION

We investigate the feasibility of PT and compare the inversion performance with crosshole seismic tomography (ST) for homogeneous and heterogeneous reservoirs. Relations between the inverted parameters (the mixed diffusivity and P-wave velocity) and the $\rm CO_2$ saturation as used by these two methods are comparable. Both are fast and computationally efficient because they are eikonal-based. However, because different signals are processed, these two approaches can be complementary to each other for characterizing an evolving $\rm CO_2$ plume shape and for evaluating the $\rm CO_2$ saturation.

In our scenarios, the upper and lower boundary of the reservoir can only be detected using ST. The PT cannot be used in the impermeable

caprock. The ST is less suitable to resolve the smaller internal contrasts in the layered reservoir. Better results when reconstructing the heterogeneity of the reservoir can be obtained by PT because it directly links to aquifer permeability. The capability for resolving the plume shape is distinct for PT and ST due to the different features of the traveltimes. First, the contrast of diffusivity is much larger than seismic velocity. Therefore, the hydraulic traveltimes used for the inversion change by orders of magnitude during CO₂ injection, rather than a few percent as for seismic traveltimes. This gives PT better sensitivity to the CO₂ plume. Moreover, due to the much larger traveltimes, PT requires less strict repeatability than does ST. In other words, the theoretical tolerance of the noise of PT is better. However, for PT, reservoir heterogeneity can alleviate the diffusivity contrast caused by CO₂ injection, and thus the front of the plume is hard to delineate by the diffusivity difference tomogram. ST can better resolve the lateral spreading part of the plume. Consequently, the best results are generally derived from the presented joint inversion.

By clustering and subsequent zonal calibration, the mean saturation of the plume can be determined. We demonstrate by sequential calibration strategies how the saturation of different layers can be distinguished. Again, jointly clustered structures provide best results for the various scenarios and conditions examined. However, it is not surprising that improper spatial delineation of the plume makes it difficult to properly estimate the saturation.

This study provides an insight into the capability of PT for application in heterogeneous formations and its potential for complementing the geophysical approaches. One crucial point remains: the transfer of this approach to the field. The main challenges of a field application include the technical implementation of sources and receivers in deep reservoirs, conducting interference injection tests during the course of CO2 injection, and interpreting PT or joint PT-ST results given nonideal conditions in the field. From the fieldinjection tests in several CO2 storage sites (e.g., Ketzin and Cranfield), it is clear that it is possible to conduct multilevel CO₂ injection tests and to obtain useful pressure signals. Application of such tests in tomographic arrangements to complement seismic measurements is thus a promising area for future study. Also, more geophysical approaches used for CO2 sequestration will be considered for comparing and being combined with PT, such as seismic full-waveform inversion and electrical resistance tomography.

ACKNOWLEDGMENTS

The authors are grateful to the EU 7th Framework Programme FP7 under grant no. 309067, project TRUST for the funding to this work. All the data used in this study can be accessed by requests to the corresponding author.

APPENDIX A

DISCRETIZATION OF TWO-PHASE FLOW-SIMULATION MODEL

Figure A-1 displays the 2D model used for forward simulations and pressure calibration. The extension of the model in horizontal

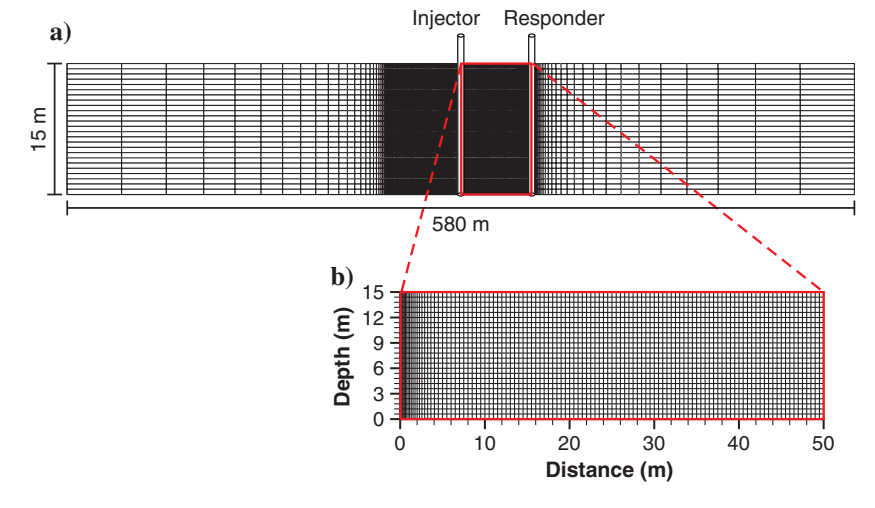


Figure A-1. Discretization of two-phase flow simulation model. (a) Full model (not to scale). (b) Magnified area between injector and responder.

direction (x-direction) is 580 m, and in the vertical direction (z-direction), it is 15 m. The injector for CO_2 and brine is placed at x=290 m, and a pressure monitoring well is 50 m away from the injector. In the x-direction, the model is discretized into 287 grid cells. Between x=240 and 340 m, the grid size is 0.5 m, with a progressive refinement to 0.09 m toward the injector. Outside of this area, the grid size increases exponentially. The largest grid size is 40 m at two lateral boundaries. In the vertical direction, the model is discretized into 25 layers, and for each, the thickness is 0.6 m.

APPENDIX B

GASSMANN-WOOD ROCK-PHYSICS MODEL

The low-frequency Gassmann equations (Gassmann, 1951) are widely used for calculating rock and fluid elastic properties in fully saturated media. The saturated bulk modulus G_{sat} is given by

$$G_{
m sat} = G_{
m dry} + rac{(1 - rac{G_{
m dry}}{G_m})^2}{rac{\phi}{G_f} + rac{1 - \phi}{G_m} - rac{G_{
m dry}}{G_m^2}},$$
 (B-1)

where $G_{\rm dry}$ and G_m are the bulk modulus of dry frame rock (drained of pore fluid) and rock matrix, respectively. Here, G_f is the bulk modulus of the pore fluid, which can be single phase or multiphase.

Bulk modulus of mixing pore fluid can be calculated by Wood's (1941) equation

$$G_f = \left(\frac{S_w}{G_w} + \frac{S_n}{G_n}\right)^{-1},\tag{B-2}$$

where G_w and G_n are the bulk modulus of brine and CO_2 , respectively. Here, G_n equals the product of the density and P-wave velocity of CO_2 . The P-wave velocity in saturated rock is then estimated by the following equations:

$$V = \sqrt{\frac{G_{\text{sat}} + \frac{4}{3}N_{\text{sat}}}{\rho_r}},$$
 (B-3)

where ρ_r is the rock density. For a CO₂-brine system, it is calculated through the linear relationship

$$\rho_r = \phi(S_w \rho_w + S_n \rho_n) + (1 - \phi)\rho_m,$$
 (B-4)

where ρ_w and ρ_n are the brine and CO₂ densities, and ρ_m is the rock-matrix density.

APPENDIX C

FULL-VELOCITY (DIFFERENCE) TOMOGRAMS

Figure C-1 shows the full velocity or velocity difference tomograms derived from ST inversion (an example of homogeneous scenario, corresponding to Figure 7I-j-7I-l). The grid size of the inversion model is 1×1 m. The dashed line delineates the reconstructed reservoir. Note that the results depicted here are slightly different in comparison with Figure 7. This is because the model grid shown in Figure 7 (ST results) is interpolated to 1×0.9375 m, to be consistent with the PT results and to implement the JT.

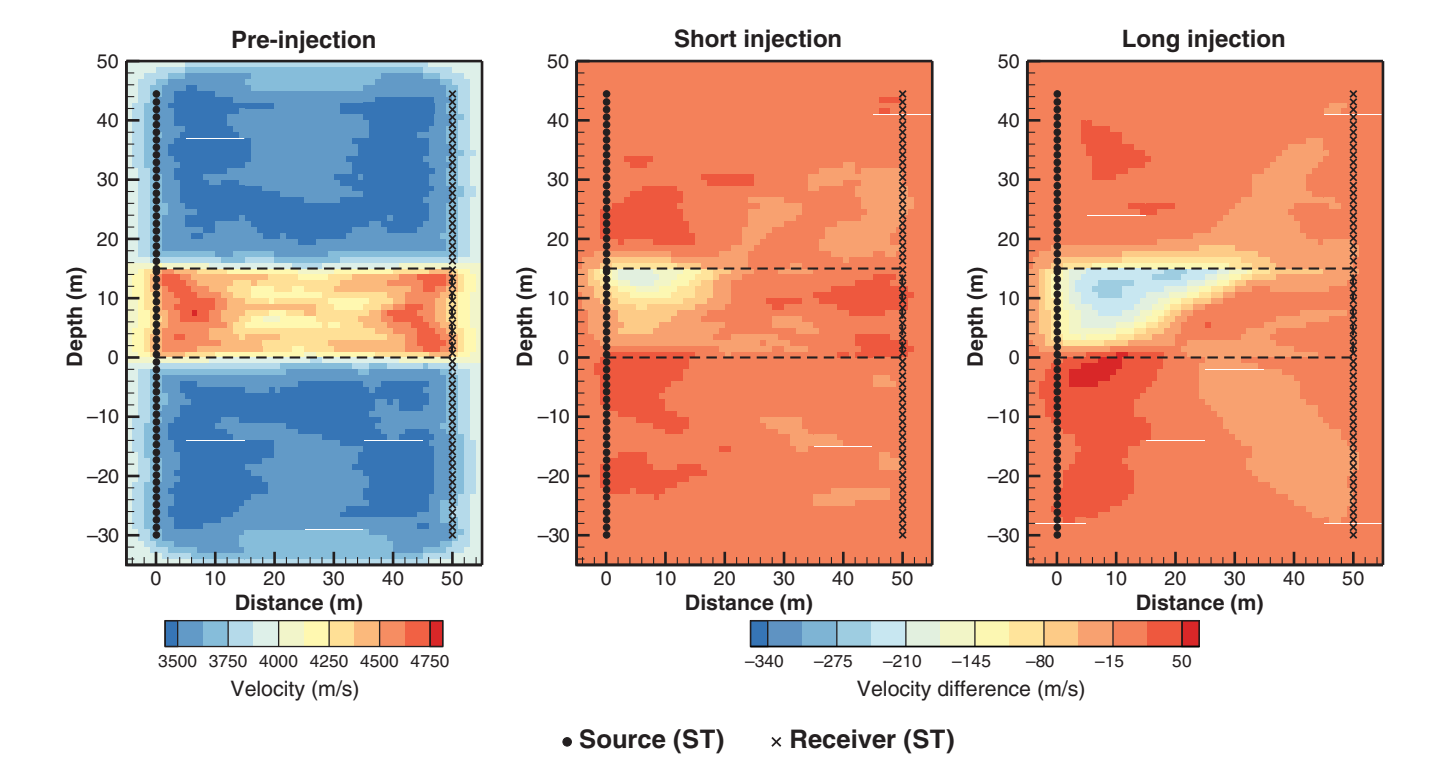


Figure C-1. Full velocity (preinjection) and velocity difference (postinjection) tomograms in homogeneous scenario. The area outlined by the dashed line indicates the reconstructed storage reservoir. Note that the sources and receivers are illustrated schematically, and their true numbers are much higher (76).

ID16 Hu et al.

NOMENCLATURE

 $\begin{array}{lll} B & = & \text{inverted plume} \\ c_n & = & \text{CO}_2 \text{ compressibility (1/Pa)} \\ c_w & = & \text{brine compressibility (1/Pa)} \\ c_p & = & \text{heat capacity (J/kgK)} \\ D & = & \text{mixed-phase diffusivity (m}^2/\text{s)} \\ D_{\text{pre}} & = & \text{diffusivity at preinjection (m}^2/\text{s)} \\ D_{\text{post}} & = & \text{diffusivity at postinjection (m}^2/\text{s)} \end{array}$

"true" plume

Α

 ΔD = diffusivity difference

 G_{dry} bulk modulus of dry frame rock (Pa) bulk modulus of mixing pore fluid (Pa) G_f bulk modulus of rock matrix (Pa) G_m = $G_{\rm sat}$ = saturated bulk modulus (Pa) integrated length in the x-direction integrated length in the z-direction kintrinsic permeability (m²) = $k_{\rm cap}$ permeability of the caprock (m²) =

 k_{ref} = intrinsic permeability of reference media (m²)

 k_{rw} = relative permeability of brine (m²) k_{rn} = relative permeability of CO₂ (m²) k_{seal} = permeability of the bottom seal (m²) K = mixed-phase conductivity (m/s) K_w = single-phase hydraulic conductivity (m/s)

 N_{dry} = shear modulus of dry frame rock (Pa)

 N_{sat} = saturated shear modulus (Pa) P_0 = pressure datum (MPa) P_d = entry pressure (Pa)

 $P_{d,\text{ref}}$ = entry pressure of reference media (Pa)

 Q_c = CO₂ injection rate (kg/s)

 $S_n = CO_2$ saturation

 S_n^{cal} = calculated CO₂ saturation S_n^{true} = "true" CO₂ saturation

 S_s = mixed-phase specific storage (1/m) S_{sw} = single-phase specific storage (1/m)

 S_w = brine saturation

 $T_{\rm inj}$ = duration of injection at CO₂ sequestration stage (h) T_s = duration of injection for multilevel CO₂ injection (h) $T_{\rm rec}$ = duration of recovery at CO₂ sequestration stage (h)

V = P-wave velocity (m/s)

 V_{post} = P-wave velocity at postinjection (m/s) V_{pre} = P-wave velocity at preinjection (m/s)

 ΔV = velocity difference (m/s) W = Lambert's function

GREEK SYMBOLS

 α = overestimation rate β = underestimation rate ε = total misclassification rate

 κ_{dry} = dry thermal conductivity (W/mK) κ_{wet} = wet thermal conductivity (W/mK)

 κ_{wet} = wet thermal conductivity λ = pore-size distribution

 μ_n = CO₂ viscosity (Pa s) μ_w = brine viscosity (Pa s) ξ = saturation error

 $\rho_m = \text{rock-matrix density (kg/m}^3)$

 $\rho_n = CO_2 \text{ density (kg/m}^3)$

 ρ_r = rock density (kg/m³) ρ_w = brine density (kg/m³)

 ϕ = porosity

 ϕ_{cap} = porosity of caprock ϕ_{seal} = porosity of bottom seal

REFERENCES

Ajo-Franklin, J. B., J. Peterson, J. Doetsch, and T. M. Daley, 2013, High-resolution characterization of a CO₂ plume using crosswell seismic tomography: Cranfield, MS, USA: International Journal of Greenhouse Gas Control, **18**, 497–509, doi: 10.1016/j.ijggc.2012.12.018.

Baddeley, A. J., 1992, An error metric for binary images: International Workshop on Robust Computer Vision, 59–78.

Birkholzer, J., Q. Zhou, and C. Tsang, 2009, Large-scale impact of CO₂ storage in deep saline aquifers: A sensitivity study on pressure response in stratified systems: International Journal of Greenhouse Gas Control, 3, 181–194, doi: 10.1016/j.ijggc.2008.08.002.
Brauchler, R., J.-T. Cheng, P. Dietrich, M. Everett, B. Johnson, R. Liedl, and

Brauchler, R., J.-T. Cheng, P. Dietrich, M. Everett, B. Johnson, R. Liedl, and M. Sauter, 2007, An inversion strategy for hydraulic tomography: Coupling travel time and amplitude inversion: Journal of Hydrology, 345, 184–198, doi: 10.1016/j.jhydrol.2007.08.011.
Brauchler, R., R. Hu, L. Hu, S. Jiménez, P. Bayer, P. Dietrich, and T. Ptak,

Brauchler, R., R. Hu, L. Hu, S. Jiménez, P. Bayer, P. Dietrich, and T. Ptak, 2013, Rapid field application of hydraulic tomography for resolving aquifer heterogeneity in unconsolidated sediments: Water Resources Research, 49, 2013–2024, doi: 10.1002/wrcr.20181.

Brauchler, R., R. Liedl, and P. Dietrich, 2003, A travel time based hydraulic tomographic approach: Water Resources Research, 39, 1370, doi: 10 .1029/2003WR002262.

Brooks, R. H., and A. T. Corey, 1964, Hydraulic properties of porous media: Hydrology papers: Colorado State University.

Burdine, N. T., 1953, Relative permeability calculations from pore size distribution data: Journal of Petroleum Technology, 5, 71–78, doi: 10.2118/225-G.

Cardiff, M., W. Barrash, and P. Kitanidis, 2013, Hydraulic conductivity imaging from 3-D transient hydraulic tomography at several pumping/observation densities: Water Resources Research, 49, 7311–7326, doi: 10.1002/wrcr.20519.

Caspari, E., T. M. Müller, and B. Gurevich, 2011, Time-lapse sonic logs reveal patchy CO₂ saturation in-situ: Geophysical Research Letters, 38, L13301, doi: 10.1029/2011GL046959.

Chadwick, A., V. Clochard, N. Delephine, K. Labat, S. Sturton, M. Buddensiek, M. Dillen, M. Nickel, A. L. Lima, G. Williams, F. Neele, R. Arts, and G. Rossi, 2010, Quantitative analysis of time-lapse seismic monitoring at the Sleipner CO₂ storage operation: The Leading Edge, 29, 170–177, doi: 10.1190/1.3304820.

Cihan, A., Q. Zhou, and J. T. Birkholzer, 2011, Analytical solutions for pressure perturbation and fluid leakage through aquitards and wells in multi-layered-aquifer systems: Water Resources Research, 47, 1–62, doi: 1010/9/2010/WR009138

Daley, T. M., J. B. Ajo-Franklin, and C. Doughty, 2011, Constraining the reservoir model of an injected CO₂ plume with crosswell CASSM at the Frio-II brine pilot: International Journal of Greenhouse Gas Control, 5, 1022–1030, doi: 10.1016/j.ijggc.2011.03.002.

Doetsch, J., M. B. Kowalsky, C. Doughty, S. Finsterle, J. B. Ajo-Franklin, C. R. Carrigan, X. Yang, S. D. Hovorka, and T. M. Daley, 2013, Constraining CO₂ simulations by coupled modeling and inversion of electrical resistance and gas composition data: International Journal of Greenhouse Gas Control, 18, 510–522, doi: 10.1016/j.ijggc.2013.04.011.

Doetsch, J., N. Linde, and A. Binley, 2010a, Structural joint inversion of time-lapse crosshole ERT and GPR traveltime data: Geophysical Research Letters, 37, L24404, doi: 10.1029/2010GL045482.

Doetsch, J., N. Linde, İ. Coscia, S. A. Greenhalgh, and A. G. Green, 2010b, Zonation for 3D aquifer characterization based on joint inversions of multimethod crosshole geophysical data: Geophysics, 75, no. 6, G53–G64, doi: 10.1190/1.3496476.

Doherty, J., 2010, PEST: Model-independent parameter estimation: Water-mark Numerical Computing.Doughty, C., B. M. Freifeld, and R. C. Trautz, 2008, Site characterization for

Doughty, C., B. M. Freifeld, and R. C. Trautz, 2008, Site characterization for CO₂ geologic storage and vice versa: The Frio brine pilot, Texas, USA as a case study: Environmental Geology, 54, 1635–1656, doi: 10.1007/ s00254-007-0942-0.

Duan, Z., J. Hu, D. Li, and S. Mao, 2008, Densities of the CO_2 -H₂O and CO_2 -H₂O-NaCl systems up to 647 K and 100 MPa: Energy Fuels, **22**, 1666–1674, doi: 10.1021/ef700666b.

Erlström, M., T. Roetting, C. Sperber, V. Shtivelman, and D. Scadeanu, 2011, Report on property values and parameters, related uncertainties,

- http://www.co2mustang.eu/PDF/Deliverables/WP02/MUSTANG_D023.pdf, accessed 14 June 2017.
- Fenghour, A., W. A. Wakeham, and V. Vesovic, 1998, The viscosity of carbon dioxide: Journal of Physical and Chemical Reference Data, 27, 31–44, doi: 10.1063/1.556013.
- Gassmann, F., 1951, Über die Elastizität poroser Medien: Veirteljahrsschrift der Naturforschenden Gesellschaft in Zürich, **96**, 1–23.
- Global CCS Institute, 2015, The global status of CCS: 2015, Summary Re-
- Gottlieb, J., and P. Dietrich, 1995, Identification of the permeability distribution in soil by hydraulic tomography: Inverse Problems, 11, 353-360,
- doi: 10.1088/0266-5611/11/2/005.

 Hammond, G. E., P. C. Lichtner, and R. T. Mills, 2014, Evaluating the performance of parallel subsurface simulators: An illustrative example with PFLOTRAN: Water Resources Research, **50**, 208–228, doi: 10.1002/wrcr
- Hao, Y., T. Yeh, and J. Xiang, 2008, Hydraulic tomography for detecting fracture zone connectivity: Ground Water, 46, 183–192, doi: 10.1111/j
- Harbaugh, A. W., 2005, MODFLOW-2005, the U. S. Geological Survey modular groundwater model — The groundwater flow process: U.S. Geological Survey Techniques and Methods 6–A16.
- Hu, L., P. Bayer, P. Alt-Epping, A. Tatomir, M. Sauter, and R. Brauchler, 2015, Time-lapse pressure tomography for characterizing CO₂ plume evolution in a deep saline aquifer: International Journal of Greenhouse Gas Control, **39**, 91–106, doi: 10.1016/j.ijggc.2015.04.013.

 Hu, L., P. Bayer, and R. Brauchler, 2016, Detection of carbon dioxide
- leakage during injection in deep saline formations by pressure tomography: Water Resources Research, **52**, 5676–5686, doi: 10.1002/
- Hu, R., R. Brauchler, M. Herold, and P. Bayer, 2011, Hydraulic tomography analog outcrop study: Combining traveltime and steady shape inversion: Journal of Hydrology, **409**, 350–362, doi: 10.1016/j.jhydrol.2011.08.031. Illman, W. A., X. Liu, S. Takeuchi, T.-C. J. Yeh, K. Ando, and H. Saegusa,
- 2009, Hydraulic tomography in fractured granite: Mizunami Underground Research site, Japan: Water Resources Research, 45, W01406,
- Ivandic, M., C. Juhlin, S. Lüth, P. Bergmann, A. Kashubin, D. Sopher, A. Ivanova, G. Baumann, and J. Henninges, 2015, Geophysical monitoring at the Ketzin pilot site for CO₂ storage: New insights into the plume evolution: International Journal of Greenhouse Gas Control, 32, 90–105, doi:
- Jackson, M. J., and D. R. Tweeton, 1996, 3DTOM: Three-dimensional geo-
- physical tomography: U.S. Department of the Interior.

 Jiménez, S., R. Brauchler, and P. Bayer, 2013, A new sequential procedure for hydraulic tomographic inversion: Advances in Water Resources, 62, 59-70, doi: 10.1016/j.advwatres.2013.10.002
- Jiménez, S., R. Brauchler, R. Hu, L. Hu, S. Schmidt, T. Ptak, and P. Bayer, 2015, Prediction of solute transport in a heterogeneous aquifer utilizing hydraulic conductivity and specific storage tomograms: Water Resources Research, **51**, 5504–5520, doi: 10.1002/2014WR016402.
- Leverett, M. C., W. B. Lewis, and M. E. True, 1941, Dimensional-model studies of oil-field behavior: Transactions of the AIME, 146, 175-193,
- Liu, X., W. A. Illman, A. J. Craig, J. Zhu, and T. J. Yeh, 2007, Laboratory sandbox validation of transient hydraulic tomography: Water Resources Research, 43, W05404, doi: 10.1029/2006WR00514
- MacQueen, 1967, Some methods for classification and analysis of multivariate observations: Proceedings of 5th Berkeley Symposium on Mathematical Statistics and Probability, 1.
- Martinez-Landa, L., T. S. Rötting, J. Carrera, A. Russian, M. Dentz, and B. Cubillo, 2013, Use of hydraulic tests to identify the residual CO₂ saturation at a geological storage site: International Journal of Greenhouse Gas Control, 19, 652–664, doi: 10.1016/j.ijggc.2013.01.043.

 Mayko, G., T. Mukerji, and J. Dvorkin, 2009, The rock physics handbook:
- Cambridge University Press.
- Calibringe Oniversity Fress.

 Nakajima, T., O. Nishizawa, and Z. Xue, 2014, Characterization on reservoir complex and CO₂ plume with V_P/V_S: Case study at Nagaoka site, Japan: Energy Procedia, **63**, 2961–2968, doi: 10.1016/j.egypro.2014.11.318.

 Niemi, A., J. Bensabat, V. Shtivelman, K. Edlmann, P. Gouze, L. Luquot, F.
- Hingerl, S. M. Benson, P. A. Pezard, K. Rasmusson, T. Liang, F. Fagerlund, M. Gendler, I. Goldberg, A. Tatomir, T. Lange, M. Sauter, and B. Freifeld, 2016, Heletz experimental site overview, characterization and data analysis for CO₂ injection and geological storage: International Journal of Greenhouse Gas Control, **48**, 3–23, doi: 10.1016/j.ijggc.2015.12
- Nordbotten, J. M., M. A. Celia, and S. Bachu, 2004, Analytical solutions for leakage rates through abandoned wells: Water Resources Research, 40, W04204, doi: 10.1029/2003WR002997.
- Nowak, W., and O. A. Cirpka, 2004, A modified Levenberg-Marquardt algorithm for quasi-linear geostatistical inversing: Advances in Water Resources, 27, 737–750, doi: 10.1016/j.advwatres.2004.03.004.

- Paradis, D., E. Gloaguen, R. Lefebvre, and B. Giroux, 2015, Resolution analysis of tomographic slug test head data: Two-dimensional radial case: Water Resources Research, **51**, 2356–2376, doi: 10.1002/2013WR014785.
- Podvin, P., and I. Lecomte, 1991, Finite difference computation of travel-times in very contrasted velocity models: A massively parallel approach and its associated tools: Geophysical Journal International, **105**, 271–284, doi: 10.1111/j.1365-246X.1991.tb03461.x.
- Pratt, R., and R. Shipp, 1999, Seismic waveform inversion in the frequency domain. Part 2: Fault delineation in sediments using crosshole data: Geophysics, 64, 902-914, doi: 10.1190/1.1444598.
- Rasmusson, K., M. Rasmusson, F. Fagerlund, J. Bensabat, Y. Tsang, and A. Niemi, 2014, Analysis of alternative push-pull-test-designs for determining in situ residual trapping of carbon dioxide: International Journal of Greenhouse Gas Control, 27, 155–168, doi: 10.1016/j.ijggc.2014.05
- Ringrose, P., M. Atbi, D. Mason, M. Espinassous, Ø. Myhrer, M. Iding, A. Mathieson, and I. Wright, 2009, Plume development around well KB-502 at the In Salah CO₂ storage site: First Break, 27, 85-89.
- Schön, J. H., 2011, Physical properties of rocks: Elsevier.
- Schöniger, A., W. Nowak, and H. J. Hendricks Franssen, 2012, Parameter estimation by ensemble Kalman filters with transformed data: Approach and application to hydraulic tomography: Water Resources Research, 48, W04502, doi: 10.1029/2011WR010462.
- Schwede, R. L., W. Li, C. Leven, and O. A. Cirpka, 2014, Three-dimensional geostatistical inversion of synthetic tomographic pumping and heat-tracer tests in a nested-cell setup: Advances in Water Resources, 63, 77–90, doi: 10.1016/j.advwatres.2013.11.004.
 Sharmeen, R., W. A. Illman, S. J. Berg, T. J. Yeh, Y. Park, E. A. Sudicky, and
- K. Ando, 2012, Transient hydraulic tomography in a fractured dolostone: Laboratory rock block experiments: Water Resources Research, **48**, W10532, doi: 10.1029/2012WR012216.
- Shi, J. Q., C. Imrie, C. Sinayuc, S. Durucan, A. Korre, and O. Eiken, 2013, Snøhvit CO₂ storage project: Assessment of CO₂ injection performance through history matching of the injection well pressure over a 32-months period: Energy Procedia, **37**, 3267–3274, doi: 10.1016/j.egypro.2013.06
- Somogyvári, M., P. Bayer, and R. Brauchler, 2016, Travel time based thermal tracer tomography: Hydrology and Earth System Sciences, **20**, 1885–1901, doi: 10.5194/hess-20-1885-2016.
- Span, R., and W. Wagner, 1996, A new equation of state for carbon dioxide covering the fluid region from the triple-point temperature to 1100 K at pressures up to 800 MPa: Journal of Physical and Chemical Reference Data, 25, 1509–1596, doi: 10.1063/1.555991.
- Straface, S., T. C. Yeh, J. Zhu, S. Troisi, and C. H. Lee, 2007, Sequential aquifer tests at a well field, Montalto Uffugo Scalo, Italy: Water Resources Research, 34, W07432, doi: 10.1002/2015WR017751.

 Sun, A. Y., J. Lu, B. M. Freifeld, S. D. Hovorka, and A. Islam, 2016, Using
- pulse testing for leakage detection in carbon storage reservoirs: A field demonstration: International Journal of Greenhouse Gas Control, 46,
- 215–227, doi: 10.1016/j.ijggc.2016.01.015. Vanorio, T., A. Nur, and Y. Ebert, 2011, Rock physics analysis and timelapse rock imaging of geochemical effects due to the injection of CO₂ into reservoir rocks: Geophysics, **76**, no. 5, O23–O33, doi: 10.1190/ geo2010-0390.1
- Vesnaver, A., and G. Böhm, 2000, Staggered or adapted grids for seismic tomography?: The Leading Edge, 19, 944–950, doi: 10.1190/1.1438762.
- Vilarrasa, V., 2012, Thermo-hydro-mechanical impacts of carbon dioxide (CO₂) injection in deep saline aquifers: Ph.D. thesis, Technical University of Catalonia.
- Wang, S., and P. R. Jaffe, 2004, Dissolution of a mineral phase in potable aquifers due to CO₂ releases from deep formations: Effect of dissolution kinetics: Energy Conversion and Management, **45**, 2833–2848, doi: 10 .1016/j.enconman.2004.01.002. Wang, Z., and M. J. Small, 2014, A Bayesian approach to CO_2 leakage
- detection at saline sequestration sites using pressure measurements: International Journal of Greenhouse Gas Control, 30, 188–196, doi: 10 1016/j.ijggc.2014.09.011.
- Wiese, B., J. Böhner, C. Enachescu, H. Würdemann, and G. Zimmermann, 2010, Hydraulic characterization of the Stuttgart formation at the pilot test site for CO₂ storage, Ketzin, Germany: International Journal of Greenhouse Gas Control, 4, 960–971, doi: 10.1016/j.ijggc.2010.06.013. Wood, A. B., 1941, Being an account of the physics of vibrations with spe-
- cial reference to recent theoretical and technical developments: A textbook of sound: Macmillan.
- Yeh, T.-C. J., and S. Liu, 2000, Hydraulic tomography: Development of a new aquifer test method: Water Resources Research, **36**, 2095–2105, doi: 10.1029/2000WR900114.
- Zha, Y., T. C. J. Yeh, W. A. Illman, T. Tanaka, P. Bruines, H. Onoe, and H. Saegusa, 2015, What does hydraulic tomography tell us about fractured geological media? A field study and synthetic experiments: Journal of Hydrology, **531**, 17–30, doi: 10.1016/j.jhydrol.2015

ID18 Hu et al.

Zha, Y., T. C. J. Yeh, D. Mao, J. Yang, and W. Lu, 2014, Usefulness of flux measurements during hydraulic tomographic survey for mapping hydraulic conductivity distribution in a fractured medium: Advances in Water Resources, 71, 162–176, doi: 10.1016/j.advwatres.2014.06.008. Zhang, F., C. Juhlin, C. Cosma, A. Tryggvason, and R. G. Pratt, 2012, Crosswell seismic waveform tomography for monitoring CO₂ injection: A case study from the Ketzin Site, Germany: Geophysical Journal International, 189, 629–646, doi: 10.1111/j.1365-246X.2012.05375.x.

Zhou, Y., D. Lim, F. Cupola, and M. Cardiff, 2016, Aquifer imaging with pressure waves — Evaluation of low-impact characterization through sandbox experiments: Water Resources Research, 52, 2141–2156, doi:

zhu, J., and T. J. Yeh, 2005, Characterization of aquifer heterogeneity using transient hydraulic tomography: Water Resources Research, 41, W07028, doi: 10.1029/2004WR003790.